THE PROPERTIES OF MICRON-SIZED PARTICLES DETECTED AT SATURN

BY THE VOYAGER 1 AND 2 PLASMA WAVE INSTRUMENTS

by

Dimitris Tsintikidis

An Abstract

Of a thesis submitted in partial fulfillment
of the requirements for the Doctor of
Philosophy degree in Physics
in the Graduate College of
The University of Iowa

August 1993

Thesis supervisor: Professor Donald A. Gurnett

ABSTRACT

During the Voyager 1 and 2 flybys of Saturn, the plasma wave (PWS) instrument recorded impulsive signals that have been attributed to micron-sized dust particles hitting the spacecraft. An analysis of these signals is presented in this study based on an improved model for the response of the electric antenna to dust impacts. The fundamental assumption is that the voltage induced on the antenna is proportional to the mass of the impacting particle. The impact rates and particle number densities are derived from the wideband waveform data and from the 16-channel spectrum analyzer data. Voyager 2 crossed the equatorial plane at 2.86 R_S. The primary dust distribution in this region consists of a "disk" that coincides with the equatorial plane. The north-south thickness of the "disk" is about 1000 km. A less dense "halo" surrounds the primary distribution and has a thickness of about 3500 km. The dust particle sizes are of the order of 10 μm. The maximum number density is on the order of 10^{-2} m^{-3} and the particle masses are up to a few times 10^{-9} g. Most likely the G-ring is the source of the particles since the impacts were detected close to that ring. Other sources, like nearby moons, are not ruled out. The optical depth of the region sampled by Voyager 2, as derived from the dust impacts analysis, is about 10^{-6}. Voyager 1 crossed the equatorial plane at 6.24 R_S. Voyager 1 detected a population of particles centered approximately 2500 km south of the equator plane. The north-

south thickness of the impact region is about 4000 km. The maximum particle number density is on the order of 10^{-3} m^{-3} and the particle sizes are a few microns. Possible sources of these particles are the moons Enceladus and Tethys. The optical depth computed from the dust impact data is about 10^{-6}. These results are in good agreement with photometric studies and the findings of numerical simulations.

Abstract approved: _____

Thesis supervisor

Professor, Dept. of Physics & Astronomy
Title and department

_July 28, 1993_____
Date

THE PROPERTIES OF MICRON-SIZED PARTICLES DETECTED AT SATURN

BY THE VOYAGER 1 AND 2 PLASMA WAVE INSTRUMENTS

by

Dimitris Tsintikidis

A thesis submitted in partial fulfillment
of the requirements for the Doctor of
Philosophy degree in Physics
in the Graduate College of
The University of Iowa

August 1993

Thesis supervisor: Professor Donald A. Gurnett

Graduate College
The University of Iowa
Iowa City, Iowa

CERTIFICATE OF APPROVAL

———————————————

PH.D. THESIS

———————————

This is to certify that the Ph.D. thesis of

Dimitris Tsintikidis

has been approved by the Examining Committee
for the thesis requirement for the Doctor of
Philosophy degree in Physics at the August 1993
graduation.

Thesis committee: _____
                  Thesis supervisor

                  _____
                  Member

                  _____
                  Member

                  _____
                  Member

                  _____
                  Member

                  _____
                  Member

ACKNOWLEDGEMENTS

ABSTRACT

During the Voyager 1 and 2 flybys of Saturn, the plasma wave (PWS) instrument

recorded impulsive signals that have been attributed to micron-sized dust particles hitting

the spacecraft. An analysis of these signals is presented in this study based on an

improved model for the response of the electric antenna to dust impacts. The

fundamental assumption is that the voltage induced on the antenna is proportional to the

mass of the impacting particle. The impact rates and particle number densities are

derived from the wideband waveform data and from the 16-channel spectrum analyzer

data. Voyager 2 crossed the equatorial plane at 2.86 R_S. The primary dust distribution

in this region consists of a "disk" that coincides with the equatorial plane. The north-

south thickness of the "disk" is about 1000 km. A less dense "halo" surrounds the

primary distribution and has a thickness of about 3500 km. The dust particle sizes are

of the order of 10 μm. The maximum number density is on the order of 10^{-2} m^{-3} and

the particle masses are up to a few times 10^{-9} g. Most likely the G-ring is the source

of the particles since the impacts were detected close to that ring. Other sources, like

nearby moons, are not ruled out. The optical depth of the region sampled by Voyager

2, as derived from the dust impacts analysis, is about 10^{-6}. Voyager 1 crossed the

equatorial plane at 6.24 R_S. Voyager 1 detected a population of particles centered

approximately 2500 km south of the equator plane. The north-south thickness of the

iii

impact region is about 4000 km. The maximum particle number density is on the order of 10^{-3} m^{-3} and the particle sizes are a few microns. Possible sources of these particles are the moons Enceladus and Tethys. The optical depth computed from the dust impact data is about 10^{-6}. These results are in good agreement with photometric studies and the findings of numerical simulations.

TABLE OF CONTENTS

LIST OF TABLES

LIST OF FIGURES

LIST OF ABBREVIATIONS AND USEFUL QUANTITIES

α	Charge collection coefficient
A	Effective surface (m²)
B	Magnetic field (T)
β	Instrumental constant
γ	Common mode rejection
C	Capacitance (F)
Δz	Vertical width (km)
e	Electron charge
eV	Electron volt
Φ	Plasma thermal energy (Ev)
f	Frequency (Hz)
f_{ce}	Electron cyclotron frequency (Hz)
f_{pe}	Electron plasma frequency (Hz)
h	Height (km)
Hz	Hertz
κ	Columnar number density
k	Yield constant (C/g)
kHz	Kilohertz

L	L-shell number
LECP	Low Energy Charged Particle instrument
m	Mass (g)
m*	Mass threshold (g)
MHz	Megahertz
μm	Micrometer
msec	Millisecond
n	Number density (m^{-3})
N	Total number of impacts
pF	Picofarad
PRA	Planetary Radio Astronomy
PWS	Plasma Wave Experiment
Q	Charge (C)
r	Particle radius (μm)
R	Impact rate (s^{-1})
rms	root-mean-square
RPWS	Radio and Plasma Wave Experiment
R_S	One Saturnian radius (60,330 km)
SCET	Spacecraft Event Time
T	Time interval (s)
t_D	Dead time (s)
τ_n	Pulse duration (s)

τ_{od}	Optical depth
U	Relative velocity (km/s)
V	Voltage (Volt)
V*	Voltage threshold (Volt)

CHAPTER I. INTRODUCTION

Saturn was the second planet encountered by the two Voyager spacecraft. These flybys provided very detailed data on Saturn and its ring system [Stone and Miner, 1981, 1982] and hence enriched our knowledge of the solar system. In addition a great deal of knowledge was gained about the magnetic field of the planet [Ness et al., 1981, 1982], its plasma environment [Bridge et al., 1981, 1982], and its radio and plasma wave emissions [Gurnett et al., 1981; Scarf et al., 1982; Warwick et al., 1981] among others. Neither of the spacecraft carried instruments devoted to the direct detection of dust, such as the beer-can experiment onboard Pioneer 11 [Humes, 1980]. Nevertheless, proof for the existence of dust at the vicinity of Saturn came from two sources, the imaging camera [Smith et al., 1981, 1982], and the plasma wave (PWS) instrument [Scarf et al., 1982].

Voyager 2 flew slightly outside of the Saturnian G ring at 2.86 R_S, where R_S = 60,330 km is one Saturnian radius [Stone and Miner, 1982]. During the Voyager 2 flyby, intense, impulsive signals were detected by the Plasma Wave Instrument at the ring plane crossing [Scarf et al., 1982]. The plasma wave instrument processes signals from the electric antenna in two ways. First, the 16-channel spectrum analyzer provides absolute intensities of the received signals in 16 frequency channels, and second, the wideband receiver provides waveforms of the received signals. The

spectrum of the impulsive signals extended well above the local electron plasma frequency, f_{pe}, hence the noise could not be due to plasma waves. The impulsive nature of the signals was directly confirmed by inspection of the waveforms. The impulsive nature of the noise and the close proximity to the G ring led to the conclusion that the noise was caused by the impact of dust particles on the spacecraft body [Scarf et al., 1982; Gurnett et al., 1983]. Scarf et al. [1982] derived a sound recording from the wideband data obtained at the ring plane crossing. This recording produced sounds that resembled a hailstorm. In other words, the sound recording gives the impression that Voyager 2 was being bombarded by many small particles as the spacecraft went through the ring plane of Saturn. The particles had to be small (less than 100 microns) since no serious damage to the spacecraft was detected.

The basic mechanism involved in detecting these particles by the plasma wave instrument is believed to be impact ionization. Because of the very large relative velocity between the spacecraft and the particles (on the order of a few tens of km/s), a particle that hits the spacecraft is instantly vaporized producing a small, outwardly expanding, partially ionized cloud of gas. Some of the charge in this cloud is collected by the plasma wave (and radio astronomy) antennas, thereby producing a voltage pulse on the antenna, which is detected by the plasma wave and planetary radio astronomy instruments.

The dust impacts detected by the Voyager 2 PWS instrument at Saturn have been studied extensively by Gurnett et al. [1983]. Dust impacts were recorded by the PWS

instrument in the vicinity of Uranus and Neptune as well [Gurnett et al., 1987, 1991].

Better physical principles were used in the latter two cases in order to recalculate an

important parameter, namely the charge collection coefficient α. The quantity α is a

measure of how efficiently the antennas collect part of the plasma cloud produced when

a particle impacts on the spacecraft. Because of the better understanding of the

mechanisms involved the new value differed from what was used in the past by almost

two orders of magnitude. The mass and the size of the particles were estimated by

analyzing the amplitude of the voltage pulse as recorded by the 16-channel spectrum

analyzer. Also, the wideband waveform receiver data were used to calculate the impact

rate. When the impact rate is combined with the spacecraft cross-sectional area and the

relative velocity between the spacecraft and the dust particles, the particle number

density can be calculated. Eventually a picture of the dust environment can be created

of the region that was sampled by the spacecraft (see, for example, Figure 13 of

Gurnett et al. [1991]).

While Voyager 2 flew close to the G ring, at 2.86 R_S, Voyager 1 flew farther

out, crossing the equatorial plane at 6.24 R_S, near the outer boundary of the diffuse E

ring. During the Voyager 1 equatorial plane crossing no wideband data were obtained

in the immediate vicinity of the equatorial plane. However, some of the noise recorded

by the 16-channel spectrum analyzer has been attributed to dust impacts [Kurth and

Gurnett, 1991]. When Voyager 1 flew by Saturn, the analysis of dust impacts did not

receive adequate attention, mainly because the dust signature was weak and difficult to

detect. However, some weak claims were made that part of what the PWS instrument recorded could be attributed to dust impacts [Kurth and Gurnett, 1991; Barbosa and Kurth, 1993]. During the Voyager 2 encounters with the three outer planets the plasma wave instrument recorded wideband data within and on either side of the dust rings. However, during the Voyager 1 flyby of Saturn no wideband data were recorded during the ring plane crossing. Hence, the derivation of the impact rate profile (and consequently the number density profile) was not possible by the technique developed by Gurnett et al. [1983]. To overcome this deficiency we have developed a new method of determining the impact rates by using the 16-channel spectrum analyzer data. The few wideband waveforms that are available were used to calibrate the impact rates as derived from the analyzer data.

The two outermost rings of Saturn, namely its E and G rings, contain a significant amount of particles of about 1 to 10 microns in size. Photometric studies provided information on the particle size distributions and the vertical extent and geometry of the rings [Esposito et al., 1984; Showalter et al., 1991; Showalter and Cuzzi, 1993]. The two rings are located in a strong magnetospheric environment hence the particles' dynamics are influenced by electromagnetic forces. The dust particles interaction with the Saturnian magnetosphere were studied as well [Grün et al., 1984, and references therein]. These studies showed that only for micron—sized particles do electromagnetic forces become important compared to gravitational forces. The structure of the E ring was studied thoroughly by Horanyi et al. [1992] and Hamilton

[1993], including the effects of various forces acting on it, i.e., electromagnetic and gravitational forces, solar radiation pressure. All the above studies were based on the images taken by the cameras onboard the Voyager spacecraft or on computer simulations. The only in situ measurement of the G ring dust environment was acquired by the Voyager 2 PWS instrument. The E ring was directly sampled by the Voyager 1 PWS instrument. It was the first time that the dust environment of the two rings was directly sampled at such a "fine scale".

All the above present the motivation of this study. The purpose of this thesis is to present a detailed study of the dust-attributed noise. The objectives are: (i) to provide a detailed description of the impact-generated noise; (ii) to interpret the impact noise in terms of the particles' masses, sizes as well as number densities; (iii) to compare our findings with theory and other methods of detecting dust in order to validate our methods of approach; (iv) to discuss the possible sources and sinks of the dust particles; and (v) to discuss the dust environment of Saturn.

The course of action is the following: first, the observations of the Voyager 2 encounter with Saturn are analyzed and discussed using the wideband waveform receiver data and the 16-channel spectrum analyzer data. Second, the observations of the Voyager 1 flyby are analyzed with more emphasis on the 16-channel spectrum analyzer and less on the wideband receiver data. It is necessary to approach the study in such a reverse chronological order since the analysis method differs for each

encounter and the method that pertains to the Voyager 2 flyby provides guidance for interpreting the Voyager 1 data.

CHAPTER II. THE VOYAGER PLASMA WAVE INSTRUMENT

Before describing the observations it is useful to review the operation of the
Voyager Plasma Wave System (from now on referred to as PWS). The PWS provided
the first direct measurements of wave-particle interactions and their effects at Jupiter,
Saturn, Uranus, and Neptune. The data acquired by the PWS answered fundamental
questions concerning the role of plasma waves in the magnetospheres of the four outer
planets and the interplanetary medium. The instrument measured the electric field
components of local plasma waves over the frequency range of 10 Hz to 56 kHz. The
plasma wave instrument shares two extendible electric antennas provided by the
planetary radio astronomy (PRA) investigators. The antenna elements are mounted in
a V configuration at an angle of 90 degrees with respect to each other. Each element
is 10 m long and has a diameter of 1.3 cm. For the radio astronomy measurements the
antennas are used as a pair of monopoles, while the PWS uses the same elements to
form a balanced electric dipole (the instrument responds to the voltage difference
between the two elements). The plasma wave signals are continuously processed with
a simple 16-channel spectrum analyzer. The 16-channel spectrum analyzer provides
absolute measurements of the voltage spectral densities of the received signals. The
analyzer provides a full spectral scan every 4 s. The PWS also has a wideband receiver

that uses the Voyager's high rate data capability originally designed to return the imaging data to give electric field waveforms at selected times during the encounter.

The 16-channel spectrum analyzer consists of 16 discrete filters with four frequencies per decade logarithmically spaced from 10 Hz to 56.2 kHz (i.e., 10, 17.8, 31.1, 56.2 Hz). The spectrum analyzer has two bands each with a logarithmic compressor. Each logarithmic compressor consists of a detector whose output is a voltage that is proportional to the logarithm of the input signal amplitude. The analyzer is operated in a step frequency mode which means that one channel after another is sampled until the full spectrum has been obtained. The lower and upper 8 channels are processed separately by the two logarithmic compressors and the two frequency ranges are scanned simultaneously. The filters have bandwidths of $\sim \pm 15\%$ for the lowest 8 frequencies (active filters) and $\sim \pm 7.5\%$ for the highest 8 frequencies (passive filters). The two logarithmic compressors provide output voltages (0 to 3 V) to the spacecraft data system. The time constant of the logarithmic compressor is about 50 ms for the lower 8 channels and about 42 ms for the upper 8 channels [Kurth et al, 1983]. The detection threshold varies with frequency. In terms of sine wave signals at the center frequencies of the bandpass channels, channel 1 (10 Hz) has a threshold of 1.7 μV/m and the threshold decreases to 0.3 μV/m for channel 16 (56.2 kHz).

The wideband receiver is used to provide waveforms of the received signals allowing very high spectral and temporal resolutions. The wideband receiver system has an automatic gain control (AGC) amplifier and a 4-bit analog-to-digital converter

that interfaces with the Voyager high rate telemetry link. The receiver covers the frequency range of 50 Hz to 12 kHz. Because of the large dynamic ranges involved, the AGC is used to maintain an almost constant output signal amplitude. The time constant of the AGC is 0.5 s. The output of the waveform amplifier is sampled at a rate of 28,800 samples per second in 48-s blocks called frames. Each frame contains 800 successive 60-ms subsequences. There is a 35-μsec time interval between samples. For more information on the plasma wave instrument see Scarf and Gurnett [1977].

During the Jupiter flybys, the spacecraft transmitted data back to Earth at the rate of 115 kbit/s, enabling the wideband plasma wave data to be telemetered in real time. However, the same transmission rate could not be maintained over the large distance from Saturn to Earth. Since the wideband data required 115 kbit/s, the data had to be placed on the tape recorder for later slow playback. Hence, at Saturn the wideband measurements were in competition with the images taken with the spacecraft cameras for the very restricted space on the tape recorder. The Voyager sequence design teams made every effort to find useful slots where wideband measurements could be placed on the tape recorders. However, only 87 frames were obtained in Saturn's magnetosphere for both encounters. On the average there were 7 wideband 48-s frames taken per day. The times and spacecraft locations for these frames are summarized in Tables 1 and 2 (adapted from Scarf et al. [1983]).

CHAPTER III. VOYAGER 2 OBSERVATIONS

Voyager 2 passed through the ring plane of Saturn just beyond the G ring. The ring plane crossing occurred at 0418:16 spacecraft event time (SCET) on August 26, 1981, at a radial distance of 2.86 Saturnian radii (1 R_s = 60,330 km). The trajectory of Voyager 2 is shown in Figure 1. During the ring plane crossing a very intense burst of noise was detected by both the plasma wave and radio astronomy instruments. The PWS observations are summarized in Figure 2. Figure 2 is a color spectrogram showing the intensity as a function of frequency and time. The highest intensity is in red and the lowest in blue. There is a sharp noise centered at about 0418 SCET. The noise lasts for about two minutes and extends almost to 1 MHz [Warwick et al., 1982]. Since the spectrum did not exhibit a cut off at the local plasma frequency or gyrofrequency [Scarf et al., 1982] it cannot be attributed to any known type of local plasma wave.

The maximum intensity of the noise occurred very close to the ring plane crossing. Figure 3 is a multi-channel plot of the electric field intensities as they were recorded by the 16-channel spectrum analyzer. While Figure 2 shows the general characteristics of the recorded noise, Figure 3 shows certain characteristics in more detail. The electric field intensities can be seen in each individual channel (or, equivalently, frequency). The noise was not very intense before the ring plane crossing

and it sharply peaked at the crossing by more than two orders of magnitude (see right-hand ordinate in Figure 3). Finally the noise subsided after the spacecraft went through the equatorial plane. The sharply peaked feature has essentially the same shape as those recorded during the Uranus and Neptune equator crossings [Gurnett et al., 1987, 1991]. The root-mean-square (rms) antenna voltage, V_{rms}, obtained by integrating across all channels is 0.137 volts. This value is one of the highest V_{rms} values ever recorded by either of the two Voyager plasma wave instruments. In fact, the strongest signal recorded during the planetary encounters was detected during the inbound part of the Voyager 2 trajectory at Neptune: 0.365 V. The signal in that case was also attributed to dust impacts. It should be noted that the Saturnian signal is smaller than the value of 0.248 V that Gurnett et al. [1983] originally quoted in that study. The discrepancy is attributed to a change in the calibration of the plasma wave instrument that occurred after the initial report was published. A comparison of our Figure 3 with their Figure 7 shows that the main features of the V_{rms} profile are essentially the same.

The most convincing evidence that the noise detected was caused by dust impacts came from the wideband waveform receiver in the PWS instrument [Scarf et al., 1982]. Prior to the encounter it was suspected that dust might be detected near the equator. A series of 48-s wideband frames was scheduled around the time of the equatorial plane crossing. The locations and times of the frames are shown at the top of Figure 3 (black squares). The importance of the wideband frames lies in the fact that each individual dust impact can be seen in the antenna voltage waveforms.

A typical sample of the wideband waveform receiver data is shown in Figure 4. The impact waveform usually consists of an abrupt pulse followed by a complex oscillatory recovery (ringing effect). The latter lasts up to about 10 ms. The rise time of the pulse is about 30 μs which is about the time resolution of the wideband receiver. Many of the pulses are stronger and cause clipping as can be seen in Figures 4c, d. The time constant of the automatic gain control is ~0.5 seconds, which is too slow to adjust to the rapid changes in the intensity during the impact. The automatic gain control responds only to the average signal amplitude. The clipped waveforms are caused by saturation in the receiver. The true shape of the waveform is probably best represented by unclipped pulses, i.e., Figure 4a, b. A waveform typically consists of a very rapid rise, with the first peak lasting a few tenths of a millisecond. The first peak is followed by a slightly longer second peak of opposite polarity which lasts from a large fraction of one millisecond to several milliseconds. The duration of a typical unclipped pulse is about 5 to 10 ms including its complex recovery.

Recently Sheehan et al. [1992] presented laboratory results demonstrating the interaction of a small expanding plasma cloud with a simple antenna. They concluded that pulses similar to the ones recorded by the Voyager 2 wideband receiver could be produced by an expanding plasma cloud (see the chapter on coupling mechanisms). The intensities of the pulses that Sheehan et al. [1992] studied are up to 5 to 8 Volts and the timescale of the phenomenon is of the order of a few milliseconds. The timescale of the wideband waveform receiver data is of the same order. The receiver

data conveys no information about the intensity of the original signal, hence no comparison can be made between the intensities of the signals as recorded by the wideband waveform receiver and the intensities recorded by Sheehan et al. [1992] in the lab. However, the wideband waveform receiver data is still useful because it provides the most definitive proof that an impact has occurred, and very reliable measurements of the impact rate.

Aubier et al. [1983] developed a model for the spectral noise density expected from the ionization of dust particles as they collide with a spacecraft. They made the assumption that the potential induced by the impact decays exponentially with time. Their model predicts that the spectral density of the noise should vary as f^{-4}. Figure 5 shows the voltage spectral density at the time of the maximum intensity. As can be seen the spectral density at high frequencies varies as f^{-4}, which is consistent with the PRA based results. A similar f^{-4} behavior has also been observed at Uranus and Neptune [Gurnett et al., 1987, 1991]. The above agreement between theory and data provides an additional strong indication that the noise recorded by PWS can be attributed to dust impacts.

CHAPTER IV. ANTENNA COUPLING MECHANISMS

The signals detected by the plasma wave instrument are electrical in origin, hence a mechanism is necessary to convert the mechanical energy of a dust particle impact into an electrical signal. There are three possible mechanisms that can convert mechanical energy to electrical energy: (1) microphonics, (2) direct detection of the charge of the particle hitting the spacecraft, and (3) detection of the charge released by impact ionization.

Microphonics describes the sensitivity of electrical systems to mechanical vibrations. A voltage can be induced on a charged capacitor if the plate separation is varied. A voltage can also be induced in a loop of wire if the area of the loop is changed in the presence of a magnetic field. For the Voyager 2 plasma wave receiver the main microphonic element is the antenna which can vibrate and induce a voltage because of the changing capacitance. Microphonic effects were, in fact, detected. When, for example, the Low Energy Charged Particle (LECP) instrument was rotated interference signals from the stepping motor were detected by the plasma wave instrument. It is likely that the microphonic effects result in signals at characteristic frequencies of the mechanical resonances of the spacecraft structure, which are in the range of a few hundred Hertz. No such signals were detectable in the high resolution

spectrum of the ring plane noise as is evident in Figure 3. Hence, it can be said that microphonics does not contribute to the recorded noise.

The second alternative is that the plasma wave receiver directly detected the charge of a dust particle hitting the antenna. If a plasma is hot then dust particles are charged negatively to a voltage on the order of the plasma thermal energy, $\Phi \sim kT/e$, which is about 10 eV in the neighborhood of the ring plane [Bridge et al., 1982]. Due to photoelectron emission a similar charging effect, but of opposite sign, occurs. The equilibrium potential is determined by the ultraviolet spectrum of the sun, which is 10 eV. It is evident that in both cases the potential is 10 eV. From the potential the charge on the dust particle can be shown to be:

$$Q = (4 \pi \epsilon_0 r) \Phi \tag{1}$$

where r is the radius of the particle, which is taken to be spherical. If one considers a particle with $r = 10 \mu m$ then the charge works out to be $Q = 1.1 \times 10^{-14}$ C. If such a particle strikes one of the antenna elements the voltage produced is $V = Q / C_A$. For $C_A \sim 90$ pF the corresponding antenna voltage is 1.2×10^{-4} V, which is too small compared to the recorded voltages that are three orders of magnitude higher.

The final possibility is impact ionization. Impact ionization is a fairly well understood phenomenon. When a high-velocity projectile, traveling at speeds of several kilometers per second, hits a solid object its kinetic energy is converted into heat which vaporizes both the particle and part of the target material. Temperatures of up to 10^5 K can be generated in such impacts [Hornung and Drapatz, 1981]. Because of the high

temperatures that develop, a substantial fraction of the material is ionized. The highly compressed partially ionized gas cloud expands radially outward from the impact point as shown in Figure 6. In the beginning the cloud is collision dominated, but as its density decreases a time comes where collisions are not important any more. At this time the remaining ionization escapes as an expanding cloud of plasma. The expansion of the plasma cloud is controlled by the self-consistent electric and magnetic fields that exist in the plasma. Various laboratory experiments have been performed to investigate impact ionization [McDonnell, 1978; Fechtig et al., 1978; Grün et al., 1984]. The results show that to a good approximation the charge Q released during the impact is proportional to the mass m of the impacting particle,

$$Q = k \, m \tag{2}$$

where k is a yield constant that depends on both the velocity of the particle and the composition of both the particle and the target. For the velocities involved in the Voyager 2 Saturn flyby it was shown that k = 0.21 C/g [Gurnett et al., 1983]. The relative velocity between Voyager 2 and a particle in circular orbit at the ring plane crossing was 13.82 km/s. This yield constant is typical for a dielectric particle (ice) hitting a metal (aluminum) surface. However, caution should be exercised. This yield constant can only be regarded as a rough estimate since there are uncertainties in the particle structure and composition, and other unknown factors might cause variations of as much as a factor of 10.

The next issue under consideration is the coupling of the charge pulse to the electric antenna. It is known that the impacts detected occur primarily on the spacecraft body and not on the antennas. The wideband waveforms respond to the voltage difference between the two antennas. Hence, if the impacts detected were only on the antennas, then the ratio of the number of pulses with positive polarities to the number with negative polarities should correspond to the ratio of the projected antenna areas to the incoming particle flux. During the Saturn ring plane crossing the ratio of the projected antenna areas was $A_1/A_2 = 1.82$. However, the ratio of the number of positive pulses to the number of negative pulses was $R_+/R_- = 1.13$. Since, to within the statistical uncertainty involved, the first ratio does not correspond to the second ratio, it was concluded that most of the impacts must be taking place on the spacecraft body [Gurnett et al., 1983]. The polarity of each pulse is believed to be determined by the relative proximity of the impact site to the two antennas, meaning that the antenna closest to the impact site receives the largest perturbation.

In our study the amplitude of the voltage pulse is calculated assuming that only a fraction α of the emitted charge Q is collected by one of the antennas, thereby producing a pulse of amplitude

$$V = \alpha \; \frac{Q}{C_A} \tag{3}$$

where C_A is the antenna capacity and $C_A = 90$ pF. The above relationship is illustrated schematically in Figure 6. It is highly unlikely that an impact occurs symmetrically with respect to the antenna elements, hence the charge collected by one of the elements will usually be larger than the charge collected by the other element. In this way, the polarity of receiver output will be determined by the element that has collected the largest charge. Since the rise time of the pulse is very fast (on the order of a few microseconds), a good case can be made that the charge collected by the antennas is due to electrons. The travel time of ions from the spacecraft body to the antennas is of the order of milliseconds which is too long to account for the observed rise times. In the above discussion an implicit assumption was made that the voltage pulse is caused by charge collection on the antennas. From simple geometric considerations one expects the collection coefficient to be very small, since the solid angle of the antennas is extremely small as seen from a dust impact site. The charge collection can however be influenced by the potential of the antenna, which is unknown.

Since the collection coefficient depends on the potential of the antenna as well as other unknown factors, such as the location of the impact, it is very difficult to estimate the collection coefficient α from fundamental principles. The collection coefficient was initially estimated to be possibly as high as 0.66 [Gurnett et al., 1983]. However, the method used was uncertain and subject to errors. It is useful to review our present ideas concerning the charge collection coefficient. First it is hypothesized that the receiver responds to the charge collected by the spacecraft body. Since the

plasma cloud is formed very near the surface, one expects the spacecraft body to be a very efficient collector. The charge that is collected produces a voltage pulse on the spacecraft body with an amplitude Q/C_{sc}, where C_{sc} is the spacecraft capacitance. For Voyager 2 the capacity C_{sc} is estimated to be 330 pF. The ideal situation for a differential measurement is when the plasma wave receiver doesn't respond to a voltage pulse on the spacecraft body. However imbalances do occur in the antenna and the differential amplifier. These imbalances give rise to a response. The magnitude of the voltage pulse from the receiver is

$$V = \gamma \frac{Q}{C_{sc}} \tag{4}$$

where γ is a constant called the common mode rejection. Based on preflight calibrations the common mode rejection is estimated to be $\gamma \sim 3 \times 10^{-3}$.

However, strong evidence suggests that the plasma wave instrument does not respond to the charge collected by the spacecraft body. A consequence of the common mode response is that all of the voltage pulses should be of the same sign. The recorded pulses appear to have an equal number of positive and negative polarities, which in turn implies that charge collection by the spacecraft body produces a negligible contribution to the observed pulse amplitude. The assumption about the spacecraft body being the charge collector can put a lower limit on the antenna charge collection

coefficient. The voltage given by Equation (3) should be significantly larger than the voltage given by Equation (4). It follows then that

$$\alpha \frac{Q}{C_A} \gg \gamma \frac{Q}{C_{SC}} \tag{5}$$

or

$$\alpha \gg \gamma \frac{C_A}{C_{SC}} \sim 8.2 \times 10^{-4} \tag{6}$$

The quantity α cannot exceed unity, hence the charge collection coefficient is restricted by the limits:

$$8.2 \times 10^{-4} \ll \alpha \leq 1 \tag{7}$$

Unfortunately Equation (7) is not of great use due to the broad range of its limits. Some other way must be found to narrow down the value of the charge collection coefficient.

A better estimate of the coupling coefficient is achieved by comparing the PWS measurements to the Planetary Radio Astronomy (PRA) measurements. The radio astronomy instrument uses the antenna elements as monopoles, which means that the PRA instrument has no common mode rejection ($\gamma = 1$) and responds directly to the charge collected by the spacecraft body. Equation (4) then becomes

$$V = \frac{Q}{C_{SC}} \qquad (8)$$

and provides a direct calculation of the voltage as recorded by the PRA instrument. Figure 7 shows a comparison of the peak voltage spectral densities as recorded by the PWS and PRA instruments during the Saturn ring plane crossing. The general form and slope of the spectra are very similar but the PWS intensities are seen to be lower than the PRA intensities. Unfortunately the integration times and sample rates differ for the two instruments: 50 ms and 1 sample per 4 s for PWS and 25 ms and 1 sample per 6 s for PRA. However, the differences in the integration times and the sampling rates between the two instruments are not enough to explain the offset in the voltage spectrum between the PWS and the PRA.

The offset in the voltage spectrum between the PWS and the PRA is found to be $V_{PWS} / V_{PRA} = 0.0202$. This offset is attributed to the difference in the antenna voltage response of the instruments: dipole versus monopole. Going one step further, it can be stated that the offset provides a direct determination of the average charge collection coefficient of the PWS dipole antenna, since the PRA monopole antenna responds directly to the total charge released from the dust impact. In other words, the PRA response can be used, in a way, to calibrate the PWS voltage response. Using Equations (3) and (5) for the PWS and PRA voltage, respectively, one can write

$$V_{PWS} = 0.0202 \ V_{PRA} \tag{9}$$

or

$$\alpha \ \frac{Q}{C_A} = 0.0202 \ \frac{Q}{C_{SC}} \tag{10}$$

Elimination of Q from both sides and substitution of C_A and C_{SC} with their values gives $\alpha = 0.0055$. It is observed that this value of α is consistent with the limits given by Equation (7).

The collection coefficient as derived above is smaller by almost two orders of magnitude than the value used by Gurnett et al. [1983]. The new estimate is based on a better principle and is more reliable than the value used by the aforementioned authors. The above method for deriving the collection coefficient was first implemented by Gurnett et al. [1987] for the analysis of dust at Uranus. It should be noted that α is at best a rough estimate and could still be in error by a substantial factor. Also the collection coefficient is the average result over many impacts and cannot be applied to a single impact, since α depends in a rather complicated fashion on the exact impact site which is unknown. In the past the Voyager 2 PWS data were used to study the dust environment of Saturn, Uranus, and Neptune [Gurnett et al., 1983, 1987, 1991]. Consequently, the α values for Uranus and Neptune (one for the former and two for the latter since the spacecraft sampled Neptune's equatorial plane once inbound and once outbound) were calculated as well in order to see if the values

differ substantially from encounter to encounter and to minimize the above mentioned uncertainties. The charge collection coefficient values were calculated the same way as for Saturn and are given in Table 3. The values are seen to be very similar. It was found that $\overline{\alpha}$ = 0.0078 ± 0.0021. The various values of α and the offsets for the cases of Uranus and Neptune can be seen in Figures 8-10.

The orientation of the spacecraft changed in each ring plane crossing. If the orientation of the spacecraft is such that most impacts occur near the antenna ellements then the plasma wave instrument will record large voltages. If the impacts occur away from the antennas then less charge will be detected by the antennas. If the spread in α within the the various ring plane crossings agrees with the spread in α for all the ring plane crossings this is an indication that the charge collection mechanism is not affected by the orientation of the spacecraft. However, if the spreads vary then the orientation of the spacecraft influences the outcome.

The following error analysis was performed to compare the spread of α. The function S was defined for the Saturn ring plane crossing:

$$S = \frac{V}{\sqrt{\Delta f}} f^2 \tag{11}$$

where $V/\sqrt{\Delta f}$ is the PWS or PRA voltage value indicated with crosses or squares respectively in Figure 7 and f is the frequency that corresponds to the voltage value. Next the function S was calculated for each of the PWS and PWS points (crosses and

squares respectively) that are along the solid lines in Figure 7. An average function S and its associated error was found next for both the PWS and the PRA points, namely $\overline{S}_{PWS}$ and $\overline{S}_{PRA}$. The ratio of the two is in fact the offset between the voltage spectra given by Equation (9). Equation (10) provided the charge collection coefficient. The same procedure was repeated for the other ring plane crossings (Figures 8-10). The offsets, the charge collection coefficients and the associated errors for each case can be seen in Table 3. Clearly the spread of α within the various ring plane crossings varies during the different ring plane crossings probably because the spacecraft orientation is different for each crossing hence influencing the charge collection coefficient. This error analysis provides a clear indication that the average value for the charge collection coefficient can not be used. Instead the value for Saturn is better to use (i.e., $\alpha = 0.0055$)

CHAPTER V. VOYAGER 2 IMPACT RATES

AND PARTICLE NUMBER DENSITIES

In essence, the impact noise can be characterized by two parameters: the impact rate, R, and the root-mean-square (rms) voltage V_{rms}. There are two ways for determining the impact rate. The first way is by simple visual inspection of the wideband waveform data. Since the dust impact signals exhibit such a distinct character (as can be seen in Figure 4) it is very easy to identify them. This method has its drawbacks: it is very time-consuming and the detection criteria are subjective. To improve on this method Gurnett et al. [1983] developed a computer algorithm that can count the number of impacts in the wideband waveform receiver data. The same algorithm was used in this study as well. The algorithm calculates the change between each successive pair of waveform samples and requires the slope of the two measurements to exceed a preset threshold. The counting threshold is adjusted in such a way as to give good agreement with visual identification of events such as the ones shown in Figure 4. The slope criterion often generated false alarms during the oscillatory recovery phase, especially for strongly clipped waveforms. Hence a dead time t_D was introduced after each event and it was adjusted to be longer for events with steeper slopes since the receiver took longer to recover after larger events. Because of

the dead time the true counting rate, R, must be determined from the observed counting

rate, R', using the following correction formula,

$$R = \frac{R'}{1-\overline{t}_D\ R'}$$ (12)

where $\overline{t}_D$ is the average dead time. The average dead time at Saturn is found to be

1.6 msec. Often visual inspection was used in order to ensure that the computer

algorithm gave valid results. The agreement between the two methods was very good.

The maximum counting rate was reached at the time of the equatorial plane crossing

and is $R = 334\ s^{-1}$. The impact rate profile corrected for dead time and the

uncertainties associated with the data points can be seen in Figure 11. A well defined

peak appears centered on the ring plane crossing ($z = 0$). After the peak, the impact

rate decreases gradually by an order of magnitude. Making the assumption that the

particle size distribution depends only on the distance z from the equatorial plane, then

the impact rate can be fit to a combination of Gaussian curves. For the case under

study, the following function gives a good fit (see solid line also in Figure 11)

$$R = R_0 + R_1\ exp[\ \frac{-(z-h)^2}{\Delta z_1^2}] + R_2\ exp[\ \frac{-(z-h)^2}{\Delta z_2^2}]$$ (13)

where h is the offset from the equatorial plane, Δz is a measure of the thickness of the

impact region of the respective Gaussian component. The fit parameters are $R_0 = 23$

$\pm$ 1 s^{-1}, R$_1$ = 262 $\pm$ 7 s^{-1}, R$_2$ = 50 $\pm$ 5 s^{-1}, h = 8 $\pm$ 9 km, Δz_1 = 481 $\pm$ 15 km, and Δz_2 = 1688 $\pm$ 129 km.

The optimum values of the fit parameters were obtained by minimizing the goodness of the fit χ^2 (least-square error) with respect to each of the parameters simultaneously. In the process of performing the minimization it was seen that χ^2 improved significantly when two Gaussians were used instead of one. The goodness did not improve notably when more than two Gaussians were used. The associated error of each parameter was defined to be the product of the error of each data point multiplied by the effect which that data point had on the determination of the parameter. For a complete description on the error analysis procedure used in this study see Press et al. [1989].

Having found the impact rate and using the antenna coupling mechanism discussed in the previous section the number density, n, can then be estimated. The number density, n, is related to the impact rate, R, via

$$R = n\ U\ A_{sc} \tag{14}$$

where U is the relative speed between the spacecraft and the particles and A_{sc} is the effective cross sectional area of the spacecraft body. The particles are assumed to be in Keplerian orbits. Keeping this in mind and the fact that the spacecraft velocity was practically constant during the equator crossing, U is 13.82 km/s. The effective cross sectional area of the spacecraft was calculated by Gurnett et al. [1983] to be 1.66 m^2.

The impact rates can be converted to number densities by solving Equation (14) for n. The number density profile can be seen on the right of Figure 11 and a maximum value is approximately 0.015 particles per cubic meter. The maximum value of density corresponds to average interparticle distances on the order of a few meters. There is little uncertainty in any of the quantities involved. The statistical error in the counting rate is only a few percent and the spacecraft velocity, and hence the relative speed, is known within a small fraction of a percent. The greatest uncertainty arises in the estimate of the effective area of the spacecraft. In determining the area, painted surfaces and epoxy structures (such as the high gain antenna) were not included since they have a very low yield coefficient, k, hence resulting in a negligible charge release after the impact. The effective area is believed to be accurate to about 10 to 20% which makes the number density estimate of comparable uncertainty.

CHAPTER VI.   VOYAGER 2 ANTENNA VOLTAGES

AND PARTICLE MASSES

The next step is to consider the mass threshold of the particles detected by the spacecraft. The mass detection threshold, m^*, is defined as the mass that produces the smallest observed V_{rms} voltage when it hits the spacecraft. By combining Equations (2) and (3) the mass of the particle can be related to the amplitude of the antenna voltage pulse as

$$m = \frac{C_A}{\alpha \, k} \, V \, . \tag{15}$$

The gain of the waveform receiver is adjusted continuously by the automatic gain control. The purpose is to maintain a constant rms output voltage. The threshold voltage V^* and V_{rms} are directly proportional as

$$V^* = \beta \, V_{rms} \, . \tag{16}$$

The constant β was calculated by Gurnett et al. [1983] and is $\beta = 0.51$. Combining the last two Equations one obtains

$$m^* = \frac{\beta \, C_A}{\alpha \, k} \, V_{rms} \qquad (17)$$

with $k = 0.21$ C / g. The rms antenna voltage and the mass threshold can be seen on Figure 12. At the time of the maximum impact rate the mass threshold reaches its maximum value and is about 5.4×10^{-9} g. As can be seen in Figure 12 the mass threshold varies continuously during the equator crossing due to the fact that the gain of the wideband receiver is inversely proportional to the rms voltage signal on the antenna. During the equator crossing the m* profile varied from 10^{-11} to 3.5×10^{-9} g. It was mentioned above that the peak number density is $n_{max} \sim 0.015$ m^{-3} which includes particles greater than 5.4×10^{-9} g. For a mass density of 1 g / cm^3 (typical dielectric, i.e., ice) the resulting radius is 10.9 μm. Hard dense particles, i.e., silicates, with mass density of 2 g / cm^3 have smaller radii (8.7 μm) and fluffy, less dense particles have larger radii. The uncertainties in α and k are quite high but since the particle sizes vary as the cube root of these quantities the fractional uncertainty on the sizes is reduced by a factor of three.

Another more quantitative procedure exists for calculating the particle mass from the rms antenna voltage. In this procedure it is assumed that the waveforms can be approximated by rectangular pulses of amplitude V_n and duration τ_n. The rms antenna voltage when averaged over a time interval T is given by

$$V_{rms}^2 = \frac{1}{T} \Sigma V_n^2 \, \tau_n \, . \tag{18}$$

By using (7) it is shown that

$$V_{rms}^2 = (\frac{\alpha \, k}{C_A})^2 \frac{1}{T} \Sigma m_n^2 \, \tau_n \, . \tag{19}$$

The pulse duration varies by an amount that is small compared to the amplitude variations, hence the pulse duration can be treated as constant, in other words $\tau_n = \tau$. The averaging time interval, T, can also be expressed in terms of the total number of impacts, N, as $N = R\,T$ so that Equation (19) becomes

$$V_{rms}^2 = (\frac{\alpha \, k}{C_A})^2 R \, \tau \, [\, \frac{1}{N} \Sigma m_n^2] \, . \tag{20}$$

Observing that the quantity in the brackets is just the rms mass squared, Equation (19) is finally written as

$$m_{rms} = \frac{C_A}{\alpha \, k} \frac{1}{(R\tau)^{1/2}} V_{rms} \, . \tag{21}$$

At the maximum impact rate of $R = 334$ s^{-1}, $V_{rms} = 0.137$ Volts and using $\tau = 1$ msec one finds that $m_{rms}^{max} = 1.3 \times 10^{-8}$ g. For typical ice particles the size becomes

16.4 microns. It should be kept in mind that since particles less than m* are not counted, the rms mass may be overestimated. If all the particles were counted, then R would be larger, hence m_{rms} smaller through (21).

Figure 13 is actually a combination of Figures 11 and 12. It can be seen clearly that the impact rate and the V_{rms} voltage profiles have the same general shape but the scale of the variations involved are quite different. The antenna voltage varies by more than two orders of magnitude during the ring plane crossing but the impact rate varies by only one order of magnitude. The difference in the shape of the antenna voltage curves and the impact rate profiles is an indication that the instrument is not counting all the particles. If all of the particles were being counted then the total power should be directly proportional to the counting rate, $V_{rms}^2 \propto R$.

It can also be seen that more and larger variations occur in the V_{rms} profile than in the impact rate profile. These variations are attributed to statistical fluctuations. The sample rate of the 16-channel spectrum analyzer is 4 samples per second whereas the sample rate of the waveform receiver is 28,800 samples per second. The statistical fluctuation varies inversely proportionally to the square root of the sampling rate. Hence, the statistical fluctuation in V_{rms}, $\Delta V_{rms}/V_{rms}$, is larger than the statistical fluctuation in R, $\Delta R/R$. The above considerations can explain the rather smooth density impact rate profile and the rather large fluctuations of the rms voltage profile.

CHAPTER VII. VOYAGER 1 OBSERVATIONS

A summary of the observations of Voyager 1 at Saturn can be seen in Figure 14. The Figure was adapted from Kurth and Gurnett [1991] (see their Plate 3). Among other features there is one tentatively labeled dust centered around 0410 spacecraft event time (SCET) on November 13, 1980. At that time the spacecraft was outbound at approximately 6 R_s (1 R_s = 60,330 km), just below the equatorial plane. The feature looks similar to the intense, impulsive, dust-attributed noise that has been observed during the other planetary encounters accomplished by Voyager 2 (see the dust signatures at Uranus and Neptune in Plates 4 and 5 of Kurth and Gurnett [1991]). However, the most definitive proof that dust exists in the area sampled by the spacecraft comes from the waveform data. The waveform signature of a dust impact consists of a single pulse and is unlike any known plasma wave waveform. The waveform data can also be used to determine particle impact rates and number densities, as was shown in chapter V, simply by following the technique of Gurnett et al. [1983, 1987, 1991], or Tsintikidis et al. [1993]. However, no wideband waveform frames (high resolution data) were available at the time that Voyager 1 crossed the equatorial plane of Saturn. Hence, it was not clear if the feature was a result of plasma wave activity or dust impacts or both. Barbosa and Kurth [1993] interpreted the Voyager 1 plasma wave observations at Saturn's inner magnetosphere in terms of

whistler mode and electrostatic electron cyclotron harmonic waves. These conclusions were reached when the authors theoretically calculated the critical flux of the superthermal electrons that can produce whistler-mode waves and electron cyclotron harmonic waves through a loss-cone instability. Furthermore, they concluded that a moderate anisotropy in the hot electron population exists in the equatorial region at L values ranging from 5 to 8. However, Barbosa and Kurth [1993] did not exclude the possibility that some of this noise may be caused by dust impacts. In addition, Kurth and Gurnett [1991] also suggested that a low frequency enhancement, below the electron cyclotron frequency, could be attributed to dust impacts, especially during the time interval 0400 to 0425 SCET, near the ring plane crossing. The purpose of this portion of the study is to determine what part of the enhancement in question can be attributed to dust impacts and to use the results to infer properties of the E ring.

In Figure 15 the Voyager 1 trajectory by Saturn is shown projected onto a meridional plane through the spacecraft. The spacecraft went as close to Saturn as 3.05 R_S at -39.51 degrees latitude on November 12 before it started its outbound leg. It crossed the equatorial plane at 0418:30 SCET on November 13, 1980 at 6.24 R_S. Figure 16 shows all the channels of the 16-channel spectrum analyzer for a 4-hour period centered on the equatorial plane crossing. A relatively long smooth background (about half an hour centered at approximately 0410 SCET) can be seen with a series of bursty signals superimposed on the background. There are a few similarities between the spectrum obtained at Saturn by Voyager 1 PWS and the spectra obtained

near the equatorial planes of Saturn, Uranus, and Neptune by Voyager 2 PWS [Tsintikidis et al., 1993; Gurnett et al., 1987, 1991]. The similarities are the spiky nature of the signals and the gradual increase and decrease in intensity (even though the change is slow and the intensity does not reach a very distinct maximum for the case of Voyager 1 at Saturn). The fact that the intensity decreases with increasing frequency and drops to the instrument noise level at higher frequencies (above a few kHz) is also consistent with what has been recorded by the Voyager 1 and 2 PWS instrument in the various planetary encounters. We attribute the bursty signals to dust impacts.

A color spectrogram of the 16-channel spectrum analyzer data taken over a longer period of time is shown in Figure 17. Figure 17 is similar to Figure 2. The most intense feature ranges in frequency from 10 Hz to 1 kHz, starting slightly before 0400 SCET and lasting for about 25 minutes. From now on, we will refer to this feature as the low-frequency equatorial enhancement. The duration of the enhancement above the lower hybrid frequency f_{LHR} is somewhat longer than at lower frequencies. The lower hybrid frequency is defined as $f_{LHR} = \sqrt{f_{ce}f_{ci}}$ where f_{ci} is the ion cyclotron frequency. As mentioned by Barbosa and Kurth [1993] a low-frequency equatorial enhancement exists over the entire region below the electron cyclotron frequency, a fact that makes the enhancement a good candidate for whistler-mode noise. Recall that whistler mode emissions propagate below the electron cyclotron frequency. Clearly the enhancement is not as sharply peaked as dust impacts observed at other planetary encounters (see the features labeled as dust in Plates 4 and 5 of Kurth and Gurnett

[1991]). The rapid peak in intensity and the clear definition of similar enhancements that Voyager 2 recorded at Saturn, Uranus, and Neptune were indications that the noise was due to dust. The primary difference between the Voyager 1 equatorial enhancement and the dust signatures observed by Voyager 2 at Saturn, Uranus, and Neptune are that the Voyager 1 signature is less intense and more broadly distributed in time.

As was discussed, Gurnett et al. [1983] studied a large number of wideband data frames recorded by both Voyager spacecraft (see their Table 1 and 2). Their results indicate the presence of dust throughout the Saturnian system. In addition, we know that Voyager 1 crossed the E-ring which is a diffuse ring. One can also look at the limited number of the Voyager 1 wideband receiver data frames, recorded before the equatorial plane crossing, to be further convinced that there is dust throughout the Saturn system. At the time the last frame was taken at 0326 SCET on November 13, 1980, before the equator crossing (position A in Figure 15), Voyager 1 was at a radial distance of 5.38 R_S and latitude of -4.53 degrees. A representative sample of dust impact signatures from this frame can be seen in Figure 18. Clearly they have identical characteristics to the wideband waveforms observed in the other planetary encounters of Voyager 2. Waveforms similar to Figure 18 have also been observed during the other times that wideband data were available (the day of the year and the times are shown in the first and second columns, respectively, of Table 4) during the Voyager 1 encounter with Saturn. For a complete summary of the Voyager 1 wideband impulse

rates see Table 1 of Gurnett et al. [1983]. The frames will be useful later on in calibrating the impact rates as they are derived from the 16-channel spectrum analyzer.

Further support for the fact that dust exists in the regions traversed by the Voyager 1 spacecraft can be found in Figure 19. This figure shows a 1-min average spectrum from 0413 to 0414 SCET, chosen during the time when the low-frequency equatorial enhancement is most prominent. Other 1-min intervals give similar spectra. The spectrum varies approximately as f^{-4}, in agreement with the spectra obtained by the Voyager 2 plasma wave instrument at Saturn (see Figure 4). The f^{-4} behavior of the spectral density agrees with the theoretically calculated spectral density if the signal is attributed to dust particle impacts [Aubier et al., 1983]. The existence of dust impacts in the high resolution data, the fact that the spacecraft traversed a tenuous ring, and the shape of the spectrum from the low resolution data all lead us to the conclusion that the Voyager 1 PWS instrument is responding to dust impacts near 0410 SCET as it crossed the E ring.

CHAPTER VIII. VOYAGER 1 IMPACT RATES AND

PARTICLE NUMBER DENSITIES

Next, we estimate the impact rate and the number density of the impacting particles. The number density, n, is given by Equation (13). The relative speed between Voyager 1 and particles in Keplerian, prograde, equatorial orbits is 29.3 km/s. The effective area is again 1.66 m^2. The greatest difficulty in computing the number density lies in calculating the impact rate, R. The 16-channel spectrum analyzer data, since it was the only data set available around the time of the equatorial plane crossing, must be used to derive impact rates.

We considered only the lowest 8 channels to look for impacts since no bursty signals can be seen in the higher channels. Figure 20 shows the lower 8 channels of the spectrum analyzer. The figure concentrates on the time interval where the low-frequency equatorial enhancement was most prominent. The relatively smooth background and the bursty signals are more easily seen now. The time interval in Figure 20 was divided into one-minute intervals. Each burst exceeding a preset threshold intensity value is attributed to a dust impact. The intensity threshold is indicated by the arrows in Figure 20. The criterion for choosing the threshold as 10^{-4} V/m was determined by the smooth background, which must be well below the threshold. As was mentioned before, the 16-channel spectrum analyzer is a step

frequency receiver. The stepping scheme does not allow simultaneous samples. Hence, the peaks in different channels correspond to different impacts, even if they appear to occur at the same time.

Another consideration included in the analysis was the duty cycle of the spectrum analyzer. The instrument spends 0.05 seconds at each channel times 8 channels (or 0.4 seconds) during a total of 4 seconds available for an entire spectral sweep. Hence the duty cycle was 0.10.

Another uncertainty involved is that of the number of impacts associated with each peak. As was mentioned before, the typical time scale of a dust impact as recorded by the wideband receiver is about 10 ms. Each point plotted in Figure 20 represents a ~ 50 ms measurement period during which any number of dust impacts may have occurred. However, using the impact rates derived from the wideband observations (e.g., ~ 16 s^{-1} at 0326 SCET) it is apparent that, on average, there is only about one impact per measuring period. If the rates increased significantly from 20 s^{-1}, then it is increasingly likely that 2 or more impacts can occur within a 50-ms interval, and our assumption of 1 impact per peak in Figure 20 becomes a lower limit. There is no way of telling the total number of impacts solely from the spectrum analyzer data because more than one 10-ms dust impact can occur within the same 50-ms measurement period. Throughout this study it will be assumed that each burst corresponds to a single dust impact.

After each planetary encounter the spectrum analyzer data are processed in order to remove unwanted predictable interference: for example, from the Low Energy Charged Particle (LECP) stepper motor. Hence, the contribution from predictable interference is close to zero for the signals under study. The removal of interference causes the small periodic gaps evident in Figure 20. An example of LECP interference is seen in Figure 21. The spacecraft was far from the planet and the LECP interference is shown by arrows. Even if the LECP interference is removed some unpredictable spacecraft-related interference signals do still occur. The primary source of these signals in the lower 8 channels is random thruster firings required to maintain spacecraft attitude. There is no data from the spacecraft that indicate exactly when the thruster firings occur. However, it is necessary to correct the impact rates by taking the contribution of the thruster activity into account.

To correct for thruster interference various times were considered during which the spacecraft was far from the planet (out in the solar wind) where actual dust impacts are highly unlikely. Outside of the Saturnian system, it can be assumed that the only significant source of low-frequency bursts is thruster activity. For these periods, we calculated the spurious event rates exceeding our threshold, and corrected for the duty cycle. Finally, the average spurious event rate was subtracted from the impact rate determined closer to the planet (column 4 in Table 4).

While the spacecraft was close to the planet and before it crossed the equatorial plane, there were six times during which 48-s wideband waveform data frames were

taken. At these six times the impact rates were found by visually inspecting the data frames (column 5 in Table 4). The highest impact rate occurred at 0326 SCET and was 15.87 s^{-1}. The probability of having a second impact during a 50-ms measurement is 0.6% which is a very low value. Hence, the assumption that there is only one impact per 50-ms peak is now justified. There is a slight difference between the newly derived impact rates and the ones listed in Table 1 of Gurnett et al. [1983]. In general, the new impact rates are higher than the older ones. The difference is attributed to the fact that in this study the impact rates were determined by visual inspection and actual count of events whereas in the study of Gurnett et al. [1983] the rates were determined in a very crude manner, namely by listening for individual impacts on an audio recording of the waveforms. For 5-min intervals centered at the times of the 6 wideband data recordings, we found the impact rates from the 16-channel spectrum analyzer data by counting the number of peaks that exceeded the amplitude threshold and correcting for spacecraft interference and duty cycle. The assumption was made that the impact rate does not change significantly over a period of a few minutes.

Next, the corrected impact rates from the 16-channel spectrum analyzer data and from the wideband waveform data were compared. There is a difference between the former and the latter due to the different thresholds for detecting impacts. In fact, the threshold of the former was lower than the latter since the wideband receiver is more sensitive to dust impacts than the spectrum analyzer. This is because the distinctive nature of the impact waveform allows a very reliable count of even very small

amplitude impacts. However, to assure that we are only using bursty events in the spectrum analyzer data, we had to use quite large amplitude thresholds.

The difference between the two impact rates can be explained with the aid of Figure 22. This figure shows a hypothetical distribution of the number of impacts with impact "amplitude". The impact "amplitude" is a function of dust mass, dust and target composition, relative speed and impact geometry. If the PWS instrument was able to detect all possible particles then the number of impacts would be given by the entire area under the curve in Figure 22. The waveform receiver subsystem would detect only impacts above its threshold as indicated by the hatched area labeled wideband data in the figure. Since the spectrum analyzer method has a lower sensitivity, hence higher threshold as described above, then this method would detect an even smaller fraction of the total distribution (labeled spectrum analyzer data in Figure 22). Therefore, for a reasonably regular distribution function, the difference between impact rates from the two methods should be the difference in the areas of the two hatched regions in Figure 22. This provides the rationale for scaling the spectrum-analyzer rates described below. Hence, the next logical step is to calculate the average discrepancy factor between the impact rates determined by the two methods. This way, the impact rates derived from the wideband waveform can be used to calibrate the spectrum analyzer rates. The average discrepancy factor was calculated to be 28.3 and the spectrum analyzer impact rates were multiplied by that factor. Figure 23 shows the agreement between the two impact rates after multiplying the spectrum analyzer derived rates by 28.3. Excluding

the first and third points, one can see that the agreement between the rest of the points is quite good. The first and third point discrepancies were not included in the calculation of the average discrepancy factor because of gaps in the spectrum analyzer data during the relevant time intervals. Because of the gaps the averaging intervals were not centered at the times of the wideband data frames.

A few comments are now appropriate about the response of the spectrum analyzer and its time constant. The response of the spectrum analyzer is subject only to the constraint $\Delta f \Delta t \simeq 1$ where Δf is the bandwidth and Δt is the duration of the signal. As the frequency decreases Δf decreases and Δt increases. It should be kept in mind that for the lowest 8 channels the bandwidth of the signal is $\sim \pm 15\%$ of the frequency. A signal sampled at, say 10 Hz, will take about one second to decay. Hence, this channel is effectively "active" for much longer than 50 ms and the duty cycle is greater than assumed above. At higher frequencies short duration (~ 10 ms) pulses will be underestimated or missed completely, especially if they occur early in the 50-ms measurement period. Therefore, the duty cycle in the 562 Hz channel is substantially less than assumed above. This is one of the main reasons that in the lowest 4 channels of Figure 20 a large number of bursts were detected that exceeded the preset threshold and that are substantially fewer bursts exceeding the preset threshold appear in the upper 4 channels of Figure 20. By adjusting the spectrum analyzer impact rates by the waveform receiver impact rates (see Figure 22) we compensate for any errors that the varying time constant might have introduced.

The average ratio of impact rates determined by using the wideband waveform receiver data and the 16-channel spectrum analyzer data was used to multiply the impact rates pertaining to the time from 0400 to 0425 SCET around the equatorial plane crossing of the spacecraft. This adjustment has the effect of increasing the sensitivity of the spectrum analyzer method to that which would be achievable had wideband data been available. The results are shown in Figure 24. A well defined peak can be seen when the spacecraft was about 2500 km below the equatorial plane. If one assumes that the particle distribution depends only on the distance z from the equatorial plane a series of Gaussian profiles can be used in order to fit the impact rate profile shown by the following Equation

$$R = R_0 + R_1 \exp[\frac{-(z-h)^2}{\Delta z_1^2}] \tag{22}$$

The best fit values are $R_0 = 5 \pm 1$ s^{-1}, $R_1 = 76 \pm 9$ s^{-1}, $h = -2473 \pm 152$ km, $\Delta z_1 = 2065 \pm 224$ km. The fit for the Voyager 1 impact rate profile is shown as a solid line in Figure 24. Having obtained the impact rate profile, it is easy to return to Equation (14) and derive the number density profile. The results can also be seen in Figure 24 (right scale). The peak number density is a little over 0.002 m^{-3}, and it occurs when the spacecraft is about 2500 km south of the equatorial plane.

CHAPTER IX. VOYAGER 1 ANTENNA VOLTAGES AND

PARTICLE MASSES

The mass of the particles impacting on Voyager 1 must be calculated in a different way than the Voyager 2 mass calculation. As was mentioned in the previous chapter the preset threshold intensity for detecting dust impacts was set at 10^{-4} V/m. The actual mass detection threshold for the wideband waveform receiver for detecting dust impacts is smaller than the above because the waveform receiver has a higher sensitivity, hence lower threshold, than the 16-channel spectrum analyzer, a fact that was also shown in Figure 22.

It is useful to find the equivalent mass detection threshold for the waveform receiver since the impact rate detected from the spectrum analyzer data was calibrated with impact rates derived from the wideband waveform receiver. This threshold can be used as a lower limit for the derivation of particle sizes. The V_{rms} voltage profile was calculated for a few minutes around 0326 SCET. The frame at 0326 SCET is the last time that wideband waveforms were recorded before Voyager 1 crossed the equatorial plane. The V_{rms} profile around this time is shown in Figure 25. The lowest V_{rms} value at 0326 SCET was considered to be the voltage that corresponds to the waveform receiver mass detection threshold. The lowest rms voltage was found to be about 0.005 V and is shown by an arrow in Figure 25. Next, Equation (17) was used

to calculate m*. The way the charge collection coefficient was calculated for the Voyager 2 case cannot be applied in the Voyager 1 case. This is because no clearly defined voltage spectra (similar to the ones shown in Figures 7-10) were available for the Voyager 1 ring plane crossing. Hence the average value 0.0078 of the collection coefficient was used and m* was found to be 1.41 x 10^{-12} g which corresponds to a particle of 0.70 μm. In essence the Voyager 1 wideband waveform receiver would be able to detect particles that are about 0.7 microns in size or larger had it been used during the Voyager 1 equatorial crossing of Saturn. In the Voyager 2 case the rms mass of the particles was found by using Equation (20). The same Equation will be used in the Voyager 1 case. As can be seen from the Equation the V_{rms} value is required in order to calculate the masses.

The V_{rms} can be determined with the aid of Figure 7. The rms voltage for the PWS measurements (crosses) is defined as the area under the crosses. It is obtained by integrating the voltage spectrum that the instrument recorded at some time interval. Hence, each individual frequency (or channel) contributes to the total V_{rms}. The contribution is given by the ratio V_i/V_{rms}, where V_i is the voltage recorded by the ith channel. In general the V_{rms} voltage varies for different ring plane crossings. However, the contribution of each channel to the total rms voltage remains the same as long as the general shape of the spectrum is the same. In other words, if V_{rms} is reduced V_i is also reduced in such a manner as to keep the aforementioned ratio constant . The V_{rms}^{V2} recorded by Voyager 2 reached a maximum value of 0.137 V

at the equator crossing.   A typical peak voltage value, V_i, was obtained for each of the lowest 4 channels (hence i=1 to 4) during the Voyager 2 equatorial crossing since the peaks were more pronounced in these channels. Also, because of the longer response of the narrowband filter , the instrument can more accurately measure the amplitude of short duration impulses. Next the ratios V_{rms}^{V2}/V_i were computed (see column 2 in Table 5). In essence the ratios show the inverse of the contribution to the total rms voltage profile from each frequency channel. Since the instrumentation and impact physics are identical it is expected that V_{rms}^{V1}/V_i ratio would be equal to the Voyager 2 V_{rms}^{V2}/V_i ratio. Hence, the following equality can be obtained:

$$\frac{V_{rms}^{V2}}{V_i^{V2}} = \frac{V_{rms}^{V1}}{V_i^{V1}}. \tag{23}$$

The V_i^{V1} values can be taken to be the values of the bursts that exceeded the preset threshold indicated by the arrows in Figure 20. The only unknown in Equation (23) is V_{rms}^{V1}. Hence solving Equation (23) for V_{rms}^{V1} a rough estimate of the rms voltage can be obtained in the Voyager 1 case. Four V_{rms}^{V1} values resulting from V_i^{V1} values for a four indicative bursts are shown in Table 5. The average voltage rms value is about 0.071 V. For this value the rms mass turns out to be 1.16×10^{-9} g by using Equation (20). This mass corresponds to a $6.5-\mu$m dielectric particle with $\rho = 1$ g/cm^3 or to a $5.2-\mu$m silicate with $\rho = 2$ g/cm^3.

The spikes in the spectrum analyzer data correspond to particles that are in the far right part wing of the hypothetical distribution of Figure 22. If one considers the uncertainties pertaining to the geometry of the impact, or target material i.e., gold has a yield constant that is six times larger than the yield constant of aluminum [Grün, 1984], or the impact velocity then it is certain that the particle radii become less than 5 micron. Unfortunately there is no way for obtaining more precise results from the 16-channel spectrum analyzer data. It should be mentioned that the particle radii estimated for the Voyager 1 case with the above method are rough estimates.

One can use the above method to derive in fact a V_{rms} profile using the first channel (10 Hz) for the Voyager 1 case. The first channel was chosen because a large number of bursts occur that exceed the preset threshold. The profile can be seen in Figure 26. This way we are concentrating on the background of Figure 20 or the bulk of the particle distribution. Since we are interested in the background the wild fluctuations can be ignored and a nominal value of 0.03 V can be used in Equation (20) that results to $m_{rms}=5.34 \times 10^{-10}$ g. This value corresponds to a 5.0-μm dielectric particle or to a 4.0-μm silicate. It seems that the Voyager 1 spectrum analyzer is detecting particles that are up to a few microns in radius consistent with the waveform receiver mass detection threshold. The above value should be regarded as an upper limit because it is certain that plasma wave activity contributes to the total V_{rms}. It was discussed that the time constant in the lowest channel is much higher than 50 milliseconds. Due to the high time constant and due to the fact that we have almost 16

impacts per second it is possible that the bursts result from a pile-up effect. Hence, the mass can also be seen as a cumulative mass. The above arguments make the rms mass to be smaller than the one calculated.

CHAPTER X. DISCUSSION

In the present study the observations of dust impacts by the Voyager 1 and 2 plasma wave instrument during the Saturnian ring plane crossings were described and analyzed. In this section a brief summary of the findings of the two spacecraft is given. Since the Voyager 2 data were analyzed first the findings of this spacecraft are summarized first and the Voyager 1 findings are summarized last. After the summary some general comments are made on the interpretation.

The method used in order to study the dust impact signals detected by Voyager 2 was first implemented by Gurnett et al. [1983] in the analysis of dust impacts at Saturn. It was used subsequently by Gurnett et al. [1991] and Tsintikidis et al. [1993]. The difference in this study is that a new, more accurate value of the charge collection coefficient, α, was used, thereby leading to more reliable results than the ones first obtained at Saturn by Gurnett et al. [1983]. The new Voyager 2 results indicate that the impulses detected by the plasma wave instrument were caused by particles of radius of about 10 μm (assuming that the particles are water ice). The mass threshold for detecting the above particles varied from 10^{-11} to 3.5×10^{-9} gm. The particle masses were derived from the rms antenna voltage. The dust impact rate was derived from the wideband waveform data and the number density was derived from the impact rate. The peak number density that occurred during the time of maximum impact rate was

about 0.015 particles / m^3. This density corresponds to an average interparticle distance on the order of a few meters. The maximum number density occurred at the equator crossing. The picture that emerges is of a dense "disk" of dust particles whose plane coincides closely with the equatorial plane. The north-south thickness of the impact region is $2\Delta z = 962$ km, based on the first Gaussian fit. A thinner "halo" surrounds the "disk" with a north-south thickness of $2\Delta z = 3376$ km based on the second Gaussian fit. Figure 27 shows the dust impact region encountered by Voyager 2 when it crossed the equator plane close to the G ring (indicated by Voyager 2).

The Voyager 2 observations were first analyzed by Gurnett et al. [1983]. They found that the particle sizes ranged from 0.3 to 3 μm. The new values for the particle sizes are considerably larger. The change can be attributed to the new lower estimate of the collection coefficient, α. The new α also accounts for the differences in the threshold mass, m^*. Gurnett et al. [1983] estimated the effective ring thickness to be 106 km, by using a mass distribution function. The new thickness of the "disk" is $2\Delta z = 962$ km. The difference is attributed to the new α value and to the definition of thickness. The above authors defined the thickness to be the distance which when multiplied by the peak particle density gave the total number of particles per unit area. In the current study the "disk" and the "halo" thickness estimates result from a Gaussian fit. If the "halo" thickness ($2\Delta z = 3376$ km) is considered then the new results are the same as those of Warwick et al. [1982] and Scarf et al. [1982]. This is

not surprising because both the current method and theirs take as thickness the region over which a substantial number of particles could be detected.

In the vicinity of Saturn, electromagnetic interactions involving dust arise due to the fact that small dust particles become charged by photoemission and electron collection from the ambient plasma. We performed simulations in order to see how the orbit of a charged particle varies due to the magnetic and gravitational fields of Saturn. The zonal harmonic magnetic field was used [Connerney et al., 1982] and the oblateness of the planet was included as well [Horanyi et al., 1992]. The simulations showed that the motion of larger particles, as seems to be the case in the region sampled by Voyager 2, is almost entirely dominated by gravitational forces: the particles seem to be confined in the same radial distance from which they started and no substantial latitudinal nor longitudinal excursions occur. Since the particles are large enough and since there is no substantial tilt of the magnetic field, the above results were not surprising. If the particles, however, are smaller than a few microns then electromagnetic effects become more important [Hamilton, 1993; Schaffer and Burns, 1987; Northrop and Hill, 1983].

Voyager 2 crossed the equatorial plane at 2.86 R_S, very close to the G ring. Most likely the dust particles that were detected by the plasma wave instrument are associated with this ring. By using the best fit Gaussian rate profiles or equivalently the number density profiles, the columnar number density perpendicular to the equator can be computed. The columnar number density can be shown to be $\kappa = \pi \int n dz$,

where n is the particle number density calculated from Equations (12) and (13) and z is the vertical distance. The integration was performed for about 4000 km along the Voyager 2 trajectory centered at the equatorial crossing. This was in agreement with the widths of the Gaussian functions given by Equation (12). It is found that $\kappa = 1.51$ x 10^4 particles/m^2. From the columnar number density we proceed to calculate the optical depth, τ_{od}, which is a measure of the fraction of the area covered by particles along the column. The optical depth is defined as $\tau_{od} = \int nAdz$, where A is the area of the particle. Spherical particles were assumed for the calculation. It is found that $\tau_{od} = 1.06$ x 10^{-6}. The reader should keep in mind that this value may be underestimated because it doesn't include small particles below the counting threshold. Recently, Showalter et al. [1991] presented an extended photometric study of Saturn's G-ring. They derived a steep particle size distribution function (it goes as r^{-6}). According to their method an upper limit of about 5 x 10^{-7} can be placed on the normal optical depth value for the region sampled by Voyager 2 (M. Showalter, personal communication). Our value is somewhat higher than the value of the photometric study by less than an order of magnitude. The discrepancy is not an alarming one. A possible explanation is that the region sampled by Voyager 2 may exhibit unusual properties. The PWS instrument is sensitive to local properties (at least for the case of dust) whereas the photometric study of Showalter and Cuzzi [1993] measures global properties. Another possibility would be if the particles were composed of something other than ice. The primary component of Saturn's rings is ice,

so one would expect the G-ring particles to be icy as well. A third alternative might be the uncertainty concerning the estimation of k. Since we do not know the yield constant for water ice, k had to be determined from other materials and could be off by a factor of 3 or more [Gurnett et al., 1983]. The discrepancy issue is expected to be resolved by the Cassini mission where both the Cosmic Dust Analyzer and the PWS measurements can both provide measurements of the dust environment of the planet. Gurnett et al. [1983] calculated the optical depth to be of the same order of magnitude as the value derived in the present study. The above authors derived the optical depth values by using the mass distribution function. The fact that the present optical depth value is similar to theirs is probably attributed to coincidence. In fact when the new charge collection coefficient value is used in their approach τ_{od} becomes unacceptably large (about 5×10^{-3}).

Particles of sizes similar to those detected at Saturn are destroyed relatively quickly, i.e., a few thousand years, due to shattering by collisions and sputtering by magnetospheric ions [Burns et al., 1984]. This seems to be the case for all the outer planets. Since the dust particles are lost so quickly there must be a suitable source for particle production. The G-ring, particularly due to its proximity to the spacecraft trajectory, seems to be a very appealing source. Micrometeoroid bombardment of relatively large ring particles produce small dust particles that diffuse outward. Also, nearby moons might contribute to particle production, i.e., Atlas, 1980S27, 1980S26, Janus, Epimetheus, and Mimas whose radial distances vary from 2.28 R_S to 3.08 R_S.

We would like to emphasize the fact that the r_{rms} = 14.6 μm value for the particle size

is an upper limit. It is certain that smaller particles also exist in that area. These

particles are not being detected because the voltage they are capable of inducing is

below the threshold that the PWS instrument can record. If the instrument were able

to detect all particles, then the total number of impacts, N, would have been larger

resulting in a smaller V_{rms} value in Equation 20, and, consequently a smaller m_{rms} value

in Equation 21. Other processes, like solar radiation pressure, electrostatic breakup,

stochastic charge variations or charge variations due to planetary shadow, etc., might

be responsible for transferring particles from even larger distances. The above

processes might replenish particles from the regions that lie close to the Voyager 2

path. Radiation pressure, for one, has a noticeable effect on the eccentricities of the

obits of smaller particles (Doug Hamilton, personal communication, 1992). It seems

that there is both a source and a sink of particles in the location that was sampled by

Voyager 2. All of the above suggest that the Saturnian G-ring is a very dynamic

system. Next, we comment on the Voyager 1 results.

When Voyager 1 flew by Saturn no wideband data (high resolution) frames were

taken during the ring plane crossing. Hence, the impact rate and consequently the

number density must be derived from the low resolution 16-channel spectrum analyzer

data. The new, improved value of the charge collection coefficient, α, was utilized

again. The Voyager 1 results show that the region sampled by the spacecraft is

populated primarily by micron sized particles. The effective mass detection threshold

used is of the order of 10^{-13} g. The particle impacts were detected when the spacecraft was in the vicinity of the equatorial plane and the impact rate peaked when the spacecraft was 2473 km south of the equatorial plane. The north-south thickness of the impact region was estimated to be $2\Delta z = 4130$ km, based on a Gaussian fit. At the maximum impact rate the peak number density was about 10^{-3} m^{-3} which corresponds to an average interparticle distance of the order of 10 meters. The picture that emerges from the Voyager 1 observations is that of a rather tenuous "cloud" of dust that is located south of the equatorial plane. This can also be seen graphically in Figure 27 (indicated by Voyager 1).

The difference between the method used in the Voyager 2 study and the method used in the Voyager 1 study lies in how the impact rate profile is derived (or equivalently how the impacts are detected). In the former part of the study, the wideband waveform (or high resolution) data frames were used in order to calculate impact rates due to the fact that there was a large number of such frames during the times (and locations) of interest. In the Voyager 1 case of the present study, the 16-channel spectrum analyzer (or low resolution) data set is used instead since no high resolution data frames were available during the equator plane crossing. However, the few high resolution data frames available at other times were still of use in order to calibrate the low resolution results. The current method could not have been used by, e.g., Gurnett et al. [1991] due to the uncertainty in the number of impacts responsible for each spike (see, for example, their Figure 2) since the very large impact rates lead

to a high probability of multiple impacts within a 50-ms measurement interval. The same argument holds also for the other planetary ring plane crossings by Voyager 2. It was fortunate that Voyager 1 crossed the E-ring region at a high speed and such a radial distance (6.24 R_S). The high relative speed between the particles and the spacecraft resulted in more charge being released during a dust impact (k = 2.05 C/g) hence enabling the PWS instrument to detect the impacts. The low number densities resulted in the spikes being well separated from each other. The above two reasons were responsible for the distinct nature of the spikes over the background plasma wave activity. Hence, we were able to derive the impact rate profile. The next step is to compare our findings with those of other studies.

Showalter et al. [1991] performed an extensive analysis of a large set of the photometric data of Saturn's E-ring. They concluded that the ring consists of slightly nonspherical particles whose size distribution is narrow: 1.0 (± 0.3 μm). This is comparable with our size findings (at least to order of magnitude comparisons). Furthermore, Randall [1993] concluded that the E-ring particle radii are in the range of 0.4 to 3.2 μm which in better agreement with our results. Randall [1993] derived these sizes by studying the energetic electrons in Saturn's magnetosphere.

One can again use the best-fit Gaussian profiles or, equivalently, the number density profiles in order to derive the columnar number density perpendicular to the equator plane. Numerical integration cannot be performed in this case since no V_{rms} profile is available. Hence, the columnar number density for the Voyager 1 case is

defined to be $\kappa = \pi\, n_1\, \Delta z_1$ and $\kappa = 2.08 \times 10^4$ particles/m². The quantity n_1 is the particle number density that corresponds to R_1 of Equation (12). The quantity Δz_1 is the width of the Gaussian for the Voyager 1 case. If a typical size of 4 μm is used, then the particle cross-sectional area is $A_0 = 5.02 \times 10^{-11}$ m². Hence, the optical depth becomes $\tau_{od} = A_0\, \kappa = 1.04 \times 10^{-6}$. However, again it should be kept in mind that the optical depth value is an underestimate since it doesn't include particles below the instrument counting threshold. For the location traversed by Voyager 1 the optical depth as given by the photometric study of Showalter et al. [1991] is about 2.20×10^{-6}. The optical depth value calculated in the current study is smaller than the one calculated by Showalter et al. [1991] by a factor of 2. There are several reasons that can account for the difference. The Voyager 1 cameras detected all the particles that happened to be in their field of view (global technique), while the PWS instrument detected only the particles that were along the trajectory of the spacecraft and which were above its sensitivity threshold (local technique). The reader should keep in mind that the PWS instrument responded only (in essence) to the shaded area of Figure 22 that's designated as "wideband data". Showalter et al. [1991] also estimated that the E-ring's thickness at its outer edge is about 40,000 km whereas the Voyager 1 plasma wave instrument detected a vertical extent smaller by an order of magnitude but with a broad, low density "halo". Other reasons that are responsible for the difference in the optical depth values are as follows. The uncertainty in the yield constant, k, still holds as was discussed in the Voyager 2 case. The impact geometry and site are not

well known.   Circular prograde motions are a good first order approximation; however, most of the particles are on moderately to very eccentric orbits [D. Hamilton, personal communication, 1992].   Eccentric orbits might introduce a 20% to 30% uncertainty in the relative velocity between the particles and the spacecraft and hence a comparable uncertainty in the impact rates (Equation 13). Some of the impact sites are such that the charge emitted cannot be detected, especially if the site is symmetric with respect to the antennas.   Of course, it should be kept in mind that plasma wave activity may be masking some of the dust impact generated noise.

It is widely accepted that Enceladus is the primary source of the E-ring dust particles [Showalter et al., 1991; Horanyi et al., 1992; Hamilton, 1993].   According to Showalter et al. [1991] the E-ring originates mostly from geyser-like eruptions from the surface of Enceladus.   The moon is located at 3.95 R_S and its surface is very smooth. The smoothness of the surface indicates that the moon is geologically active. Observations show that the thickness of the E-ring at its outer edge is about 40,000 km [Showalter et al., 1991].   The vertical structure of the E-ring, as it comes about from computer simulations, favors the northward asymmetry more than the southward asymmetry presented herein [D. Hamilton, personal communication, 1993].   The simulation preference is a result of the quadrupole component of the Saturnian magnetic field.   Our results show that the dust is concentrated predominantly south of the equatorial plane. The vertical extent of the dust in the model used by Hamilton [1993] barely reaches the north part of the region derived from our study. On the other hand,

the moon Tethys is located at about 4.89 R_S and lies closer (compared to Enceladus) to the location of the spacecraft ring plane crossing. It is possible that the particles whose effects were recorded by the PWS instrument could emanate from Tethys. Our model accounts for the existence of dust up to about 2500 km north of the equatorial plane (right wing of the Gaussian profile in Figure 24). The fact that our technique does not detect dust that is predicted to exist more than a few thousand kilometers north of the equator plane [Horanyi et al., 1992; Hamilton, 1993], has no obvious explanation.

A comparison of the PWS and PRA results is now appropriate. Aubier et al. [1983] attributed the noise that the PRA instrument detected during the Voyager 1 equator plane crossing to shot noise from electrons hitting the antennas. The power spectrum of shot noise goes as f^{-2} and is a smooth, broadband spectrum [Meyer-Vernet and Perche, 1989]. However, the Voyager 1 PWS observations at Saturn did not have these characteristics. First, as can be seen from Figure 5, the PWS noise exhibits bursts which are inconsistent with the smooth nature of the shot noise. Also, the power spectrum as derived from the PWS data during the equator crossing (see Figure 4) more closely approaches the f^{-4} behavior expected from dust impacts than the f^{-2} behavior expected from shot noise.

We are looking forward to the future Cassini mission to Saturn. A Radio and Plasma Wave (RPWS) instrument will be included in this mission. The spacecraft is scheduled to orbit the planet for about 60 orbits. Hence, we will have a much better

opportunity to map the dust environment of Saturn. The RPWS results can then be directly compared to the results of the Cassini Dust Analyzer onboard the same spacecraft. Furthermore, we will be able to better study "mixed" recorded signals, i.e., noise that appears to result from the combination of inherently different signals like dust-attributed noise and whistler-mode noise.

Table 1. Wideband 48-s frames recorded per day at Saturn during the Voyager 1 encounter. Shown are the times and the locations of the spacecraft at which the frames were recorded. A total of 34 frames were recorded.

Date (DOY)	SCET (Hr, Min, Sec)	Radial Distance R_S	Latitude (deg)	Longitude (deg)
Nov. 12 1980 (317)	0035:47	24.94	1.88	10.55
	0143:47	23.83	1.55	48.44
	0310:10	22.41	1.09	96.51
	0550:59	19.75	0.04	185.79
	0634:59	19.02	-0.30	210.18
	0849:22	16.79	-1.52	284.45
	1001:23	15.58	-2.32	324.08
	1257:23	12.61	-4.91	60.19
	1830:10	6.95	-15.65	234.52
	2106:58	4.45	-28.67	302.81
	2251:46	3.25	-40.39	323.94
Nov. 13 1980 (318)	0108:34	3.50	-25.06	329.91
	0326:10	5.39	-4.51	20.25
	0730:10	9.48	9.36	141.60
	1033:47	12.61	13.68	239.68
	1446:11	16.85	16.95	17.56
	1641:22	18.77	17.94	91.09
	1829:22	20.56	18.69	140.87
	2106:10	23.14	19.56	227.93
	2321:23	25.35	20.17	303.20
Nov. 14 1980 (319)	0119:47	27.27	20.62	9.21
	0306:11	29.00	20.97	68.61
	0541:23	31.50	21.42	155.34
	1610:59	41.57	22.65	147.97
Nov. 15 1980 (320)	0121:23	50.27	23.32	96.83
	0422:11	53.12	23.49	198.36
	0658:11	55.57	23.62	285.99
	0935:47	58.04	23.74	14.53
	1153:23	60.19	23.84	91.84
	1537:23	63.69	23.99	217.73
	1842:59	66.59	24.10	322.05
	2226:59	70.08	24.22	87.98
Nov. 16 1980 (321)	0058:11	72.43	24.29	172.99
	0553:23	77.02	24.42	338.99

Table 2. Same as in Table 1 but for the Voyager 2 encounter with Saturn. A total of 53 frames were taken.

Date (DOY)	SCET (Hr, Min, Sec)	Radial Distance R_S	Latitude (deg)	Longitude (deg)
Aug. 24 1981 (236)	0136:47	40.20	13.74	350.56
	0611:11	36.93	14.04	144.43
	0845:35	35.08	14.24	230.96
	1406:24	31.19	14.71	50.58
	1728:48	28.72	15.07	163.77
	2017:36	26.63	15.42	258.04
	2236:48	24.90	15.75	335.69
Aug. 25 1981 (237)	1145:35	14.76	18.97	52.25
	1146:23	14.75	18.97	52.68
	2007:11	7.84	24.43	318.63
	2007:59	7.82	24.45	319.03
	2323:59	5.02	28.48	49.32
	2324:47	5.01	28.49	49.64
Aug. 26 1981 (238)	0200:47	3.08	26.68	93.93
	0305:35	2.69	16.93	100.32
	0417:35	2.85	0.15	108.59
	0419:11	2.86	-0.20	108.86
	0420:47	2.87	-0.56	109.14
	0422:23	2.88	-0.91	109.42
	0423:59	2.89	-1.26	109.71
	0424:47	2.90	-1.43	109.85
	0559:59	3.89	-16.35	134.76
	0735:59	5.19	-23.00	171.46
	0736:47	5.20	-23.03	171.80
	0858:23	6.36	-25.69	208.20
	1811:11	14.07	-29.33	134.34
	1811:59	14.08	-29.33	134.77
	2251:11	17.77	-29.48	287.27
	2251:59	17.78	-29.48	287.71
Aug. 27 1981 (239)	0715:11	24.20	-29.46	206.09
	0715:59	24.21	-29.46	206.53
	1414:23	29.39	-29.38	79.62
	1415:11	29.40	-29.38	80.09
	2006:23	33.67	-29.31	276.31
	2007:11	33.68	-29.31	276.75

Table 2. (continued)

Aug. 28 1981 (240)	0203:59	37.97	-29.25	116.47
	0204:47	37.98	-29.25	116.92
	1210:23	45.15	-29.15	96.40
	1211:11	45.16	-29.15	96.85
	1938:23	50.39	-29.08	347.81
	1939:11	50.40	-29.08	348.26
Aug. 29 1981 (241)	1011:11	60.49	-28.98	118.02
	1011:59	60.50	-28.98	118.47
	1544:47	64.32	-28.95	305.49
	1545:35	64.33	-28.95	305.94
	2043:11	67.73	-28.92	113.21
	2043:59	67.74	-28.92	113.66
Aug. 30 1980 (242)	0044:47	70.48	-28.91	249.03
	0046:35	70.50	-28.90	250.13
	1014:23	76.94	-28.86	209.29
	1015:11	76.95	-28.86	209.74
	2059:11	84.23	-28.82	211.92
	2059:59	84.24	-28.82	212.37

Table 3. Voyager 2 charge collection coefficient values
for the outer planets.

PLANET	V_{PWS}/V_{PRA}	α_{eff}	σ_α
Saturn	0.0202	0.0055	0.0007
Uranus	0.0242	0.0066	0.0018
Neptune inbound	0.0367	0.0100	0.0006
Neptune outbound	0.0334	0.0091	0.0016

Table 4. The various impact rates (in s^{-1}) as derived from the 16-channel spectrum analyzer (SA) and the wideband waveform receiver (WFR) data at certain times (Day Of Year, DOY, and SpaceCraft Event Times, SCET) corrected for numerous effects.

DOY	SCET	SA Impact Rate	SA Impact Rate Corrected for Spacecraft Noise	WFR Impact Rate	SA Derived Equivalent WFR Rate
317	1001	0.09	0.01	5.36	0.28
317	1257	0.36	0.28	12.06	7.92
317	1830	0.17	0.09	13.57	2.55
317	2107	0.27	0.19	3.53	5.38
318	0109	0.43	0.35	5.72	9.91
318	0326	0.53	0.45	15.87	12.74

Table 5. Calculation for the Voyager 1 V_{rms} values at the lowest 4 frequencies.

Frequency (Hz)	V_{rms}^{V2}/V_i^{V2}	V_i^{V1} (V)	V_{rms}^{V1} (V)
10.0	40.48	2.1×10^{-3}	0.085
17.8	39.96	1.0×10^{-3}	0.040
31.1	41.80	9.0×10^{-4}	0.038
56.2	29.92	4.0×10^{-3}	0.120

Figure 1.   The path of Voyager 2 projected into a meridional plane passing through

the spacecraft. Voyager 2 crossed the ring plane at 2.86 R_s, very close

to the G ring. The E ring dimensions have been magnified for clarity

purposes.

A-G93-115

VOYAGER 2

A, B RING

E-RING

SATURN

G-RING

5

10
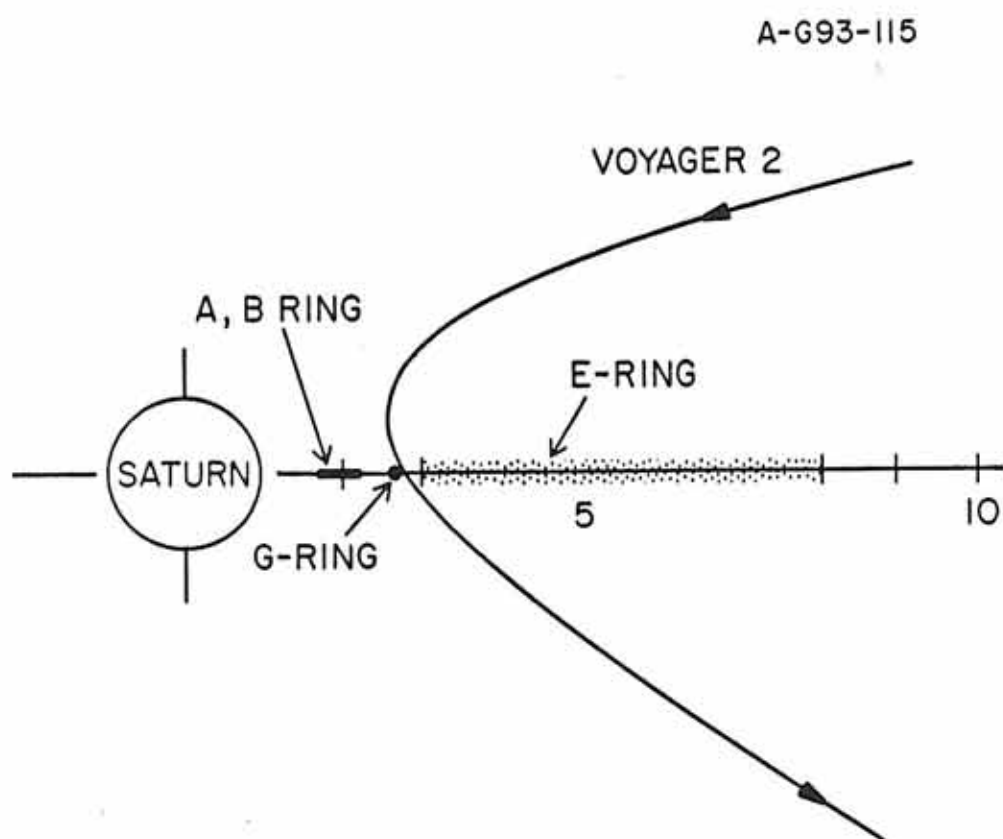
Figure 2.   Frequency-time spectrogram for the Voyager 2 encounter with Saturn. SCET is shown in the abscissa along with the radial distance and latitude of the spacecraft. A false color scheme is utilized where the highest intensities are shown in red and the lowest ones in blue. The most intense feature is attributed to dust impacts and occurred when the spacecraft crossed the equatorial plane.

B-G93-296

VOYAGER 2   SATURN
AUGUST 26, DAY 238, 1981

ELECTRIC FIELD (V/m)

-02
-03
-04
-05
-06

FREQUENCY (kHz)

10.0
1.0
0.1
0.01

f_{ce}

SCET	0405	0410	0415	0420	0425	0430
R(R_S)	2.78	2.80	2.83	2.86	2.90	2.94
LAT (DEG)	3.04	1.87	0.96	-0.38	-1.48	-2.54
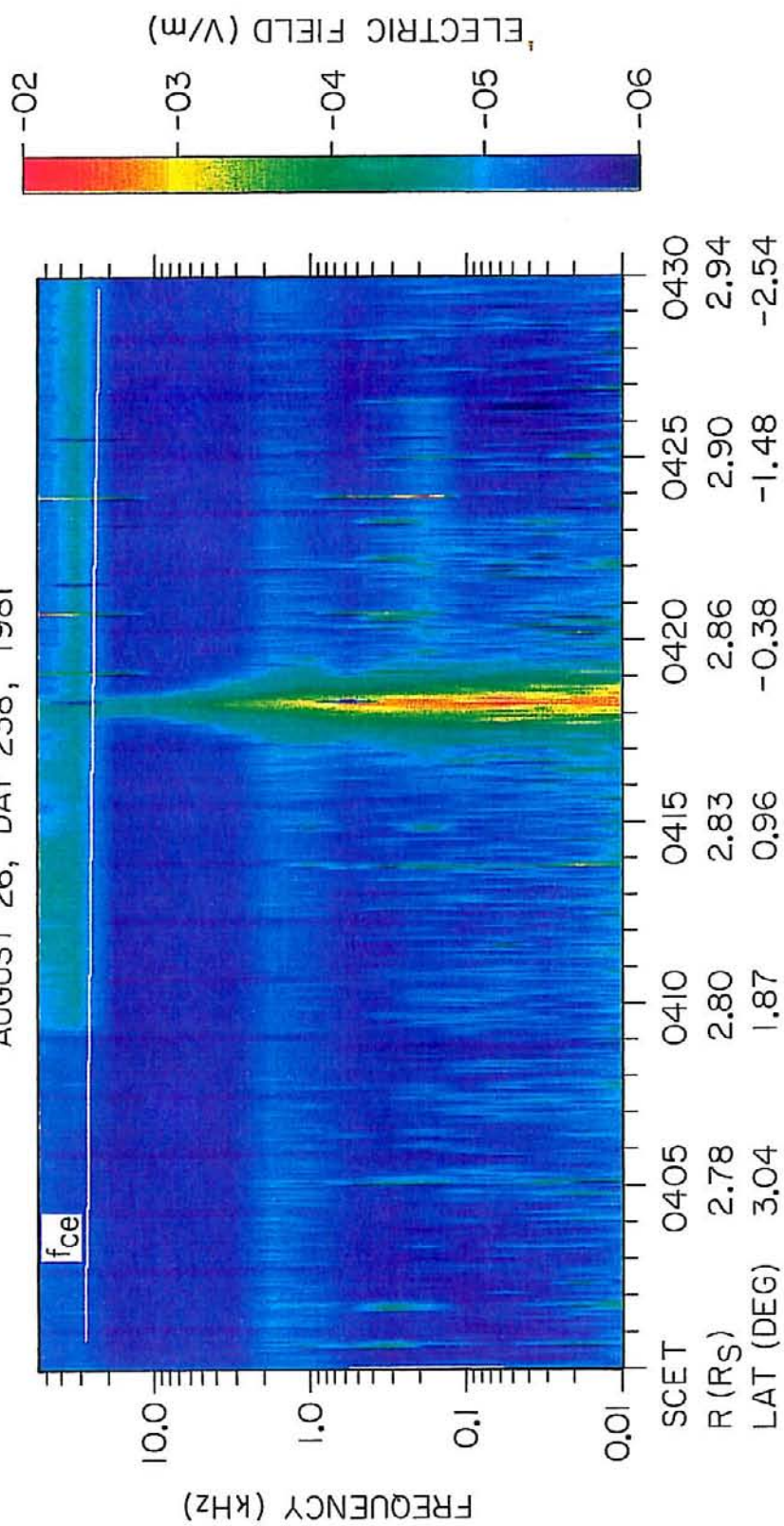
Figure 3.   The electric field intensities measured by the 16-channel spectrum

analyzer near the equatorial plane. The very intense broadband noise

observed almost exactly at the equator crossing is attributed to particles

hitting the spacecraft.

C-G92-172-1
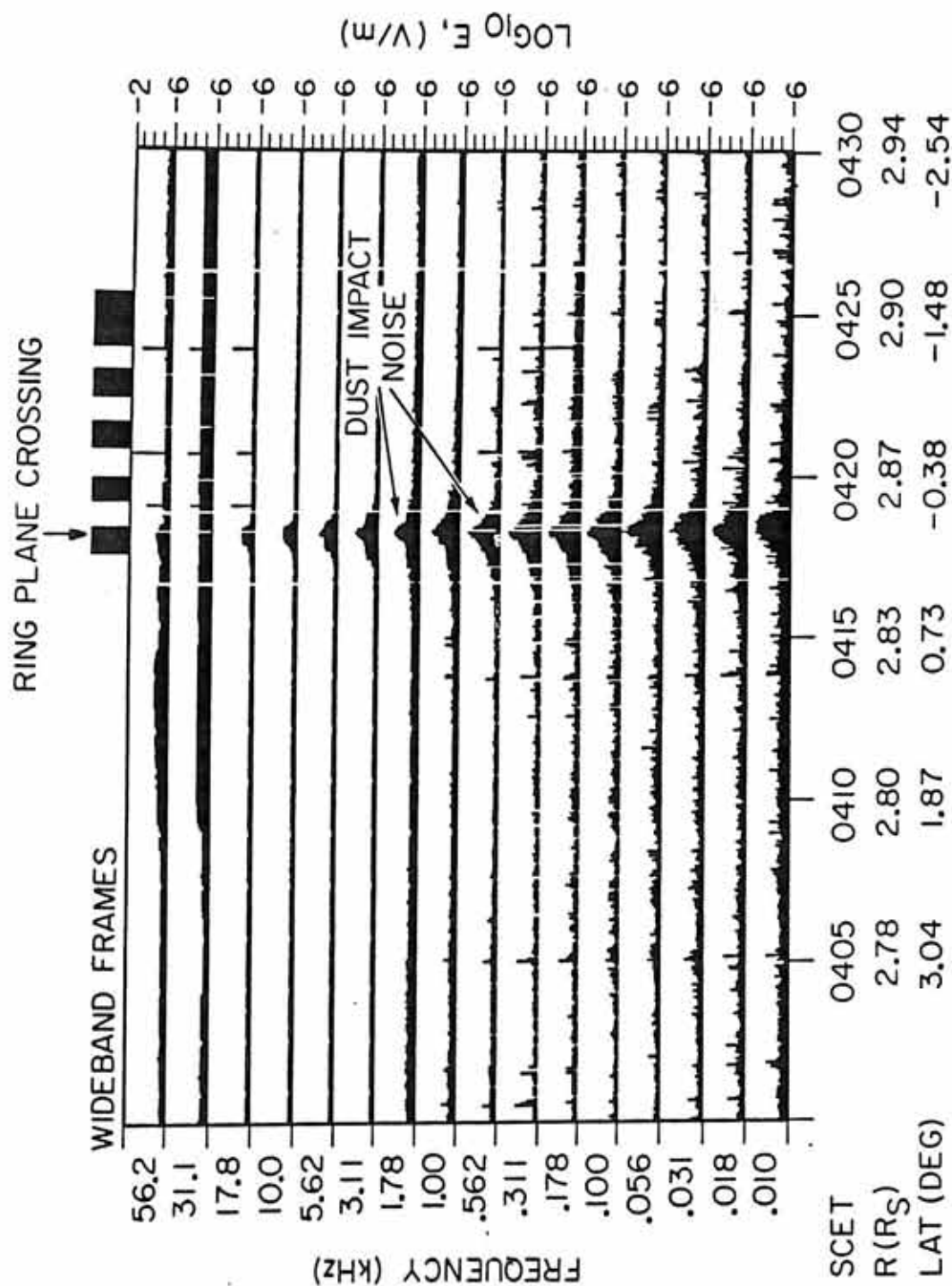
Figure 4. A series of dust impact waveforms in the vicinity of the ring plane crossing. The impacts are shown by arrows.

A-G92-178-1
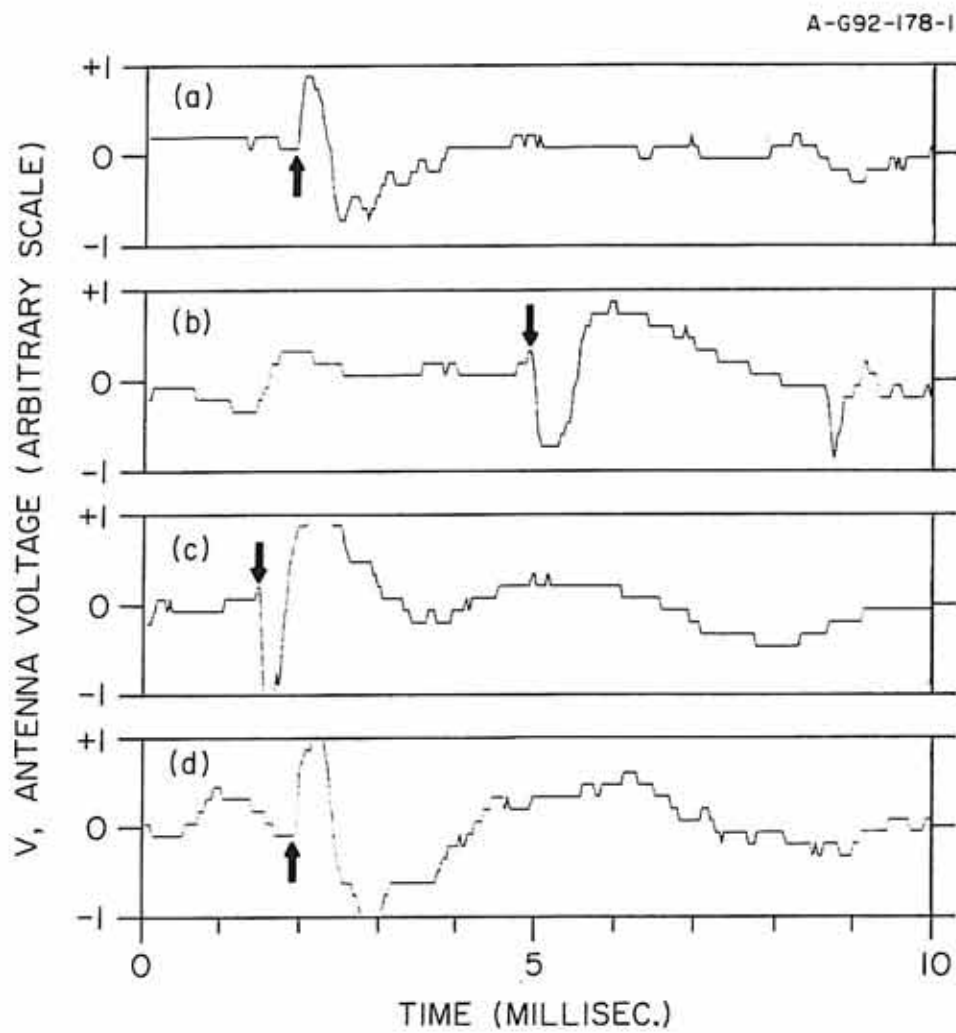
VOYAGER 2, AUGUST 26, 1981

Figure 5.   The voltage spectral density of the dust impact noise as recorded by the

plasma wave instrument close to the time of maximum intensity at the

ring plane crossing. It varies as f^{-4} at frequencies higher than a few

hundred Hertz which is consistent with the results of the Uranus and

Neptune encounters and theory [Aubier et al., 1983].

B-G92-170

$\frac{V^2}{\Delta f} \sim f^{-4}$

SATURN
DUST IMPACTS
VOYAGER 2
AUG. 26, 1981

FREQUENCY (Hz)

$\frac{V^2}{\Delta f}$, VOLTAGE SPECTRAL DENSITY (VOLTS^2 Hz^{-1})
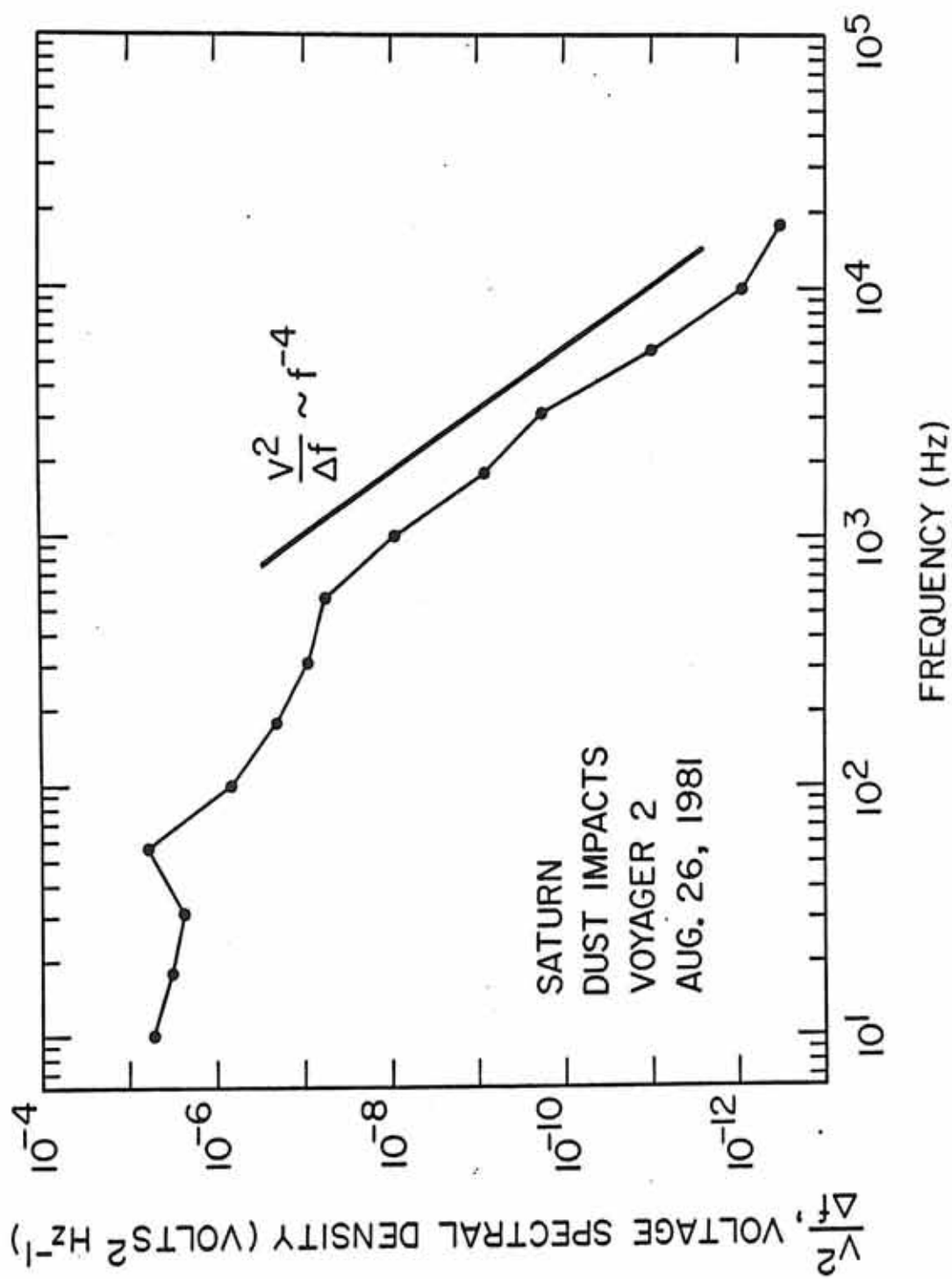
Figure 6.   Schematic illustration of the model used to analyze the voltage produced

by an impact. The spacecraft body collects the charge -Q released by

the impact and the antenna collects a fraction α of the charge, αQ. The

voltage pulse produced is $V = \alpha Q/C_A$, where C_A is the antenna

capacity, and it is detected by the antenna. Since the plasma wave

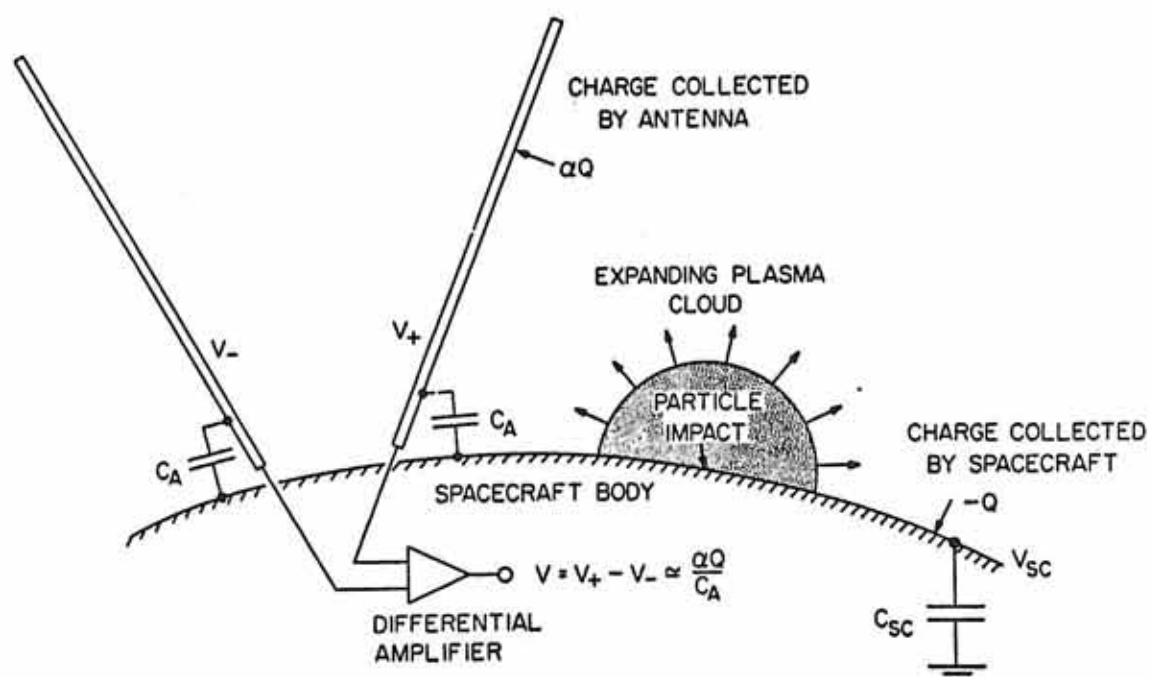instrument is a differential system, it does not respond to the charge

collected by the spacecraft body.

C-G86-807

CHARGE COLLECTED
BY ANTENNA

αQ

EXPANDING PLASMA
CLOUD

PARTICLE
IMPACT

CHARGE COLLECTED
BY SPACECRAFT

$-Q$

V_-

V_+

C_A

C_A

SPACECRAFT BODY

V_{SC}

$V = V_+ - V_- \simeq \dfrac{\alpha Q}{C_A}$

C_{SC}

DIFFERENTIAL
AMPLIFIER

Figure 7.　　Comparison of the voltage spectra detected by the Voyager 2 plasma wave and radio astronomy instruments for Saturn. The charge collection coefficient, α, can be seen in the lower left corner of the panel. The offset is caused by the different mode of electric field detection used by the two instruments (dipole vs. monopole, respectively for PWS and PRA).

A-G92-270

SATURN

VOYAGER 2
PEAK AMPLITUDES
0418-0419 SCET
AUGUST 26, 1981

PRA

OFFSET

PWS

$\alpha = 0.0055$

FREQUENCY, Hz

$V/\sqrt{\Delta f}$, VOLTS Hz$^{-1/2}$
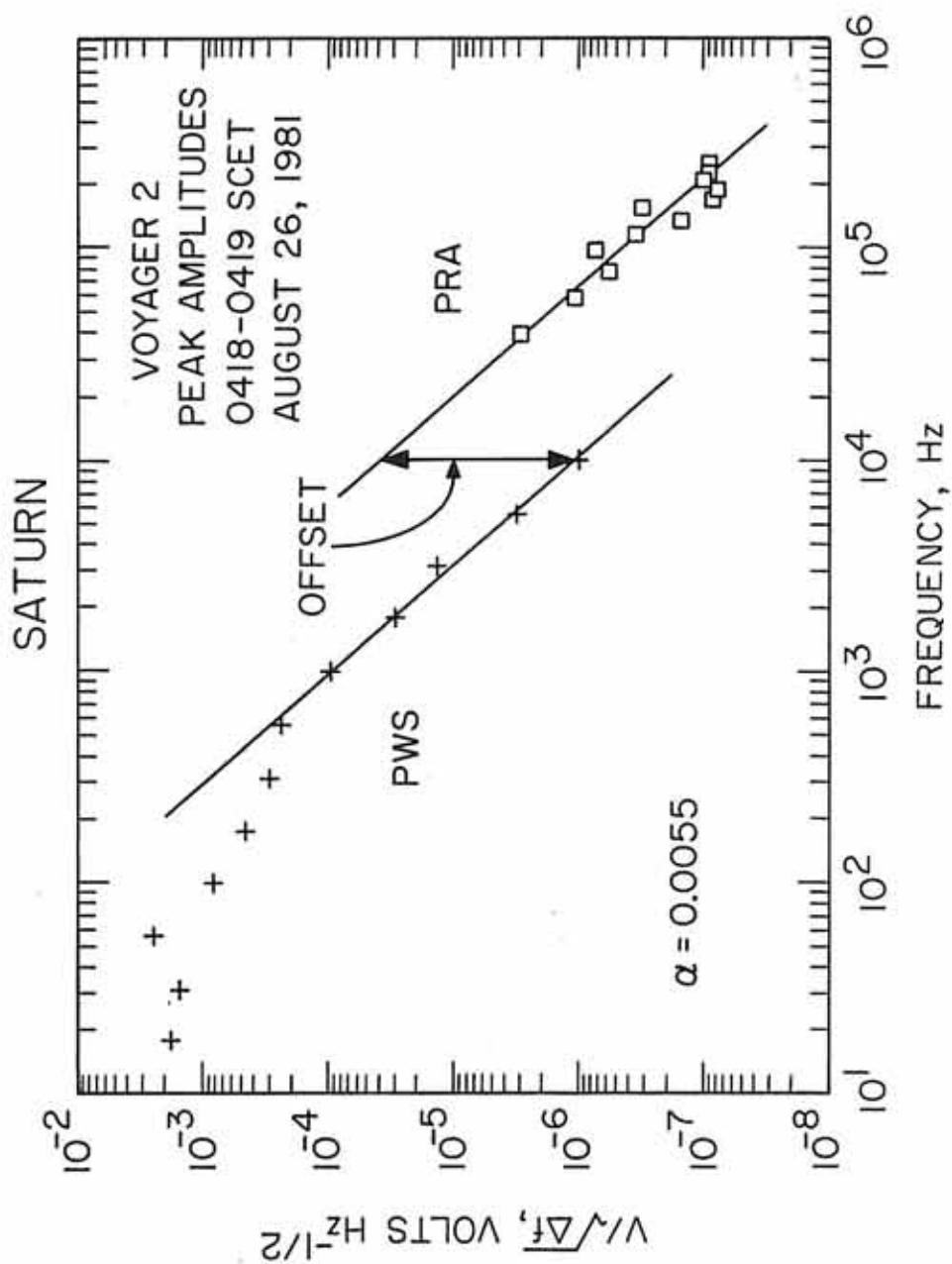
Figure 8.　　Same as in Figure 7 but for the case of Uranus.

URANUS

VOYAGER 2
PEAK AMPLITUDES
1715–1716 SCET
JANUARY 24, 1986

PRA

PWS

OFFSET

$\alpha = 0.0066$

FREQUENCY, Hz

$V/\sqrt{\Delta f}$, VOLTS Hz$^{-1/2}$

A-G87-247-1
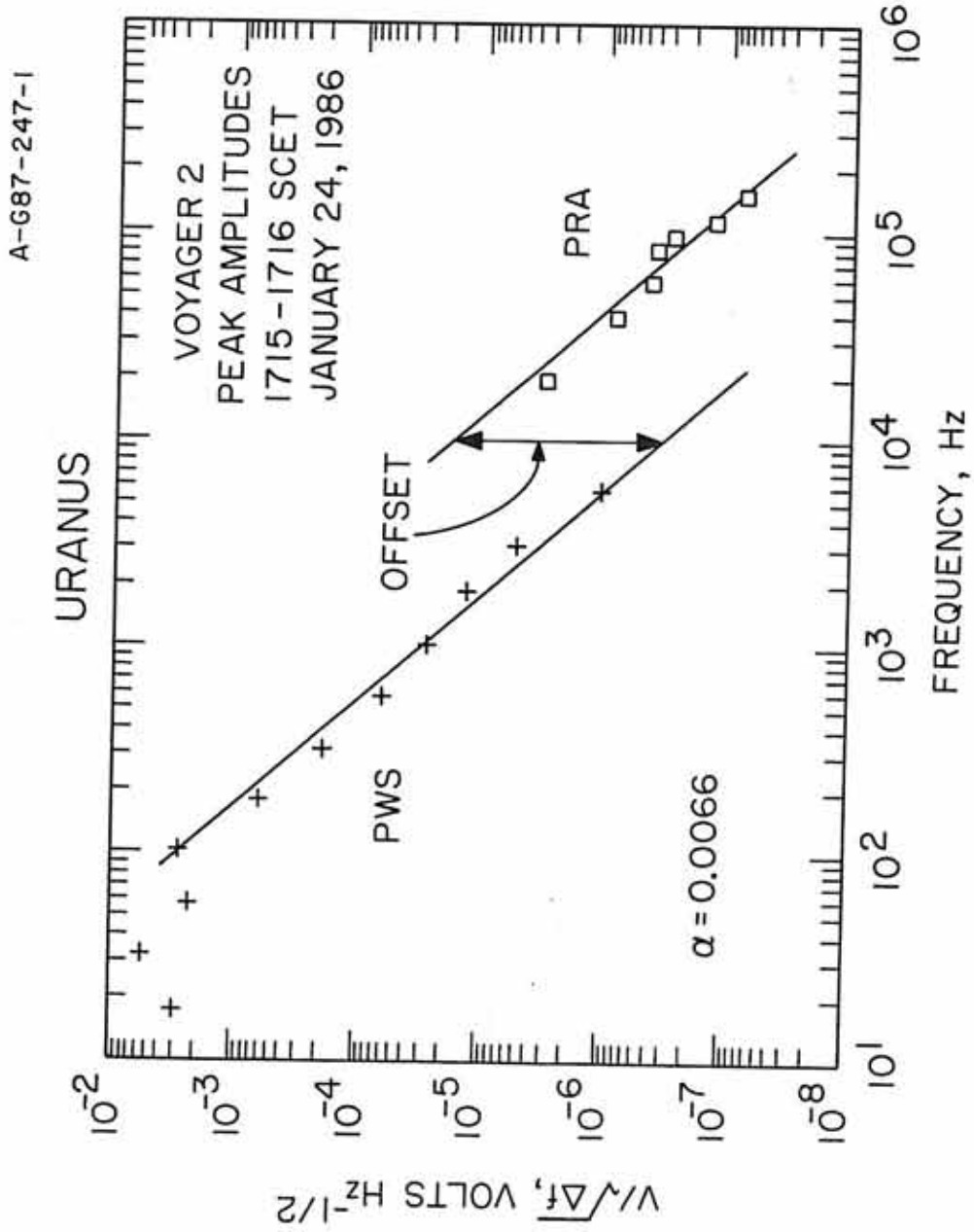
Figure 9.   Same as in Figure 7 but for the inbound case of Neptune.

NEPTUNE INBOUND

A-G92-272

VOYAGER 2
PEAK AMPLITUDES
0253-0254 SCET
AUGUST 25, 1989

PRA

OFFSET

PWS

$\alpha = 0.010$

$V/\sqrt{\Delta f}$, VOLTS Hz$^{-1/2}$

FREQUENCY, Hz
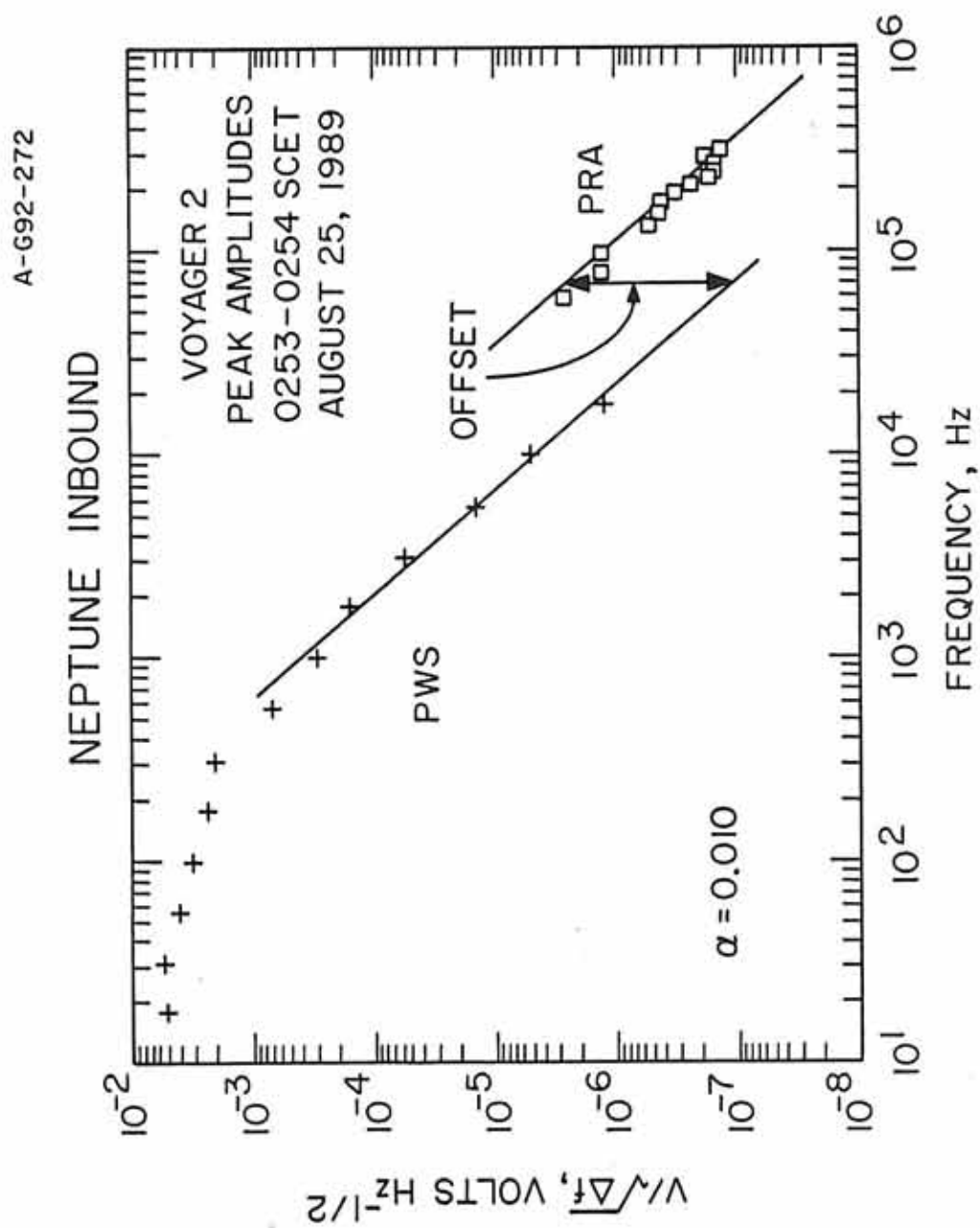
Figure 10.   Same as in Figure 7 but for the outbound case of Neptune.

NEPTUNE OUTBOUND

VOYAGER 2
PEAK AMPLITUDES
0516-0517 SCET
AUGUST 25, 1989

A-G92-271
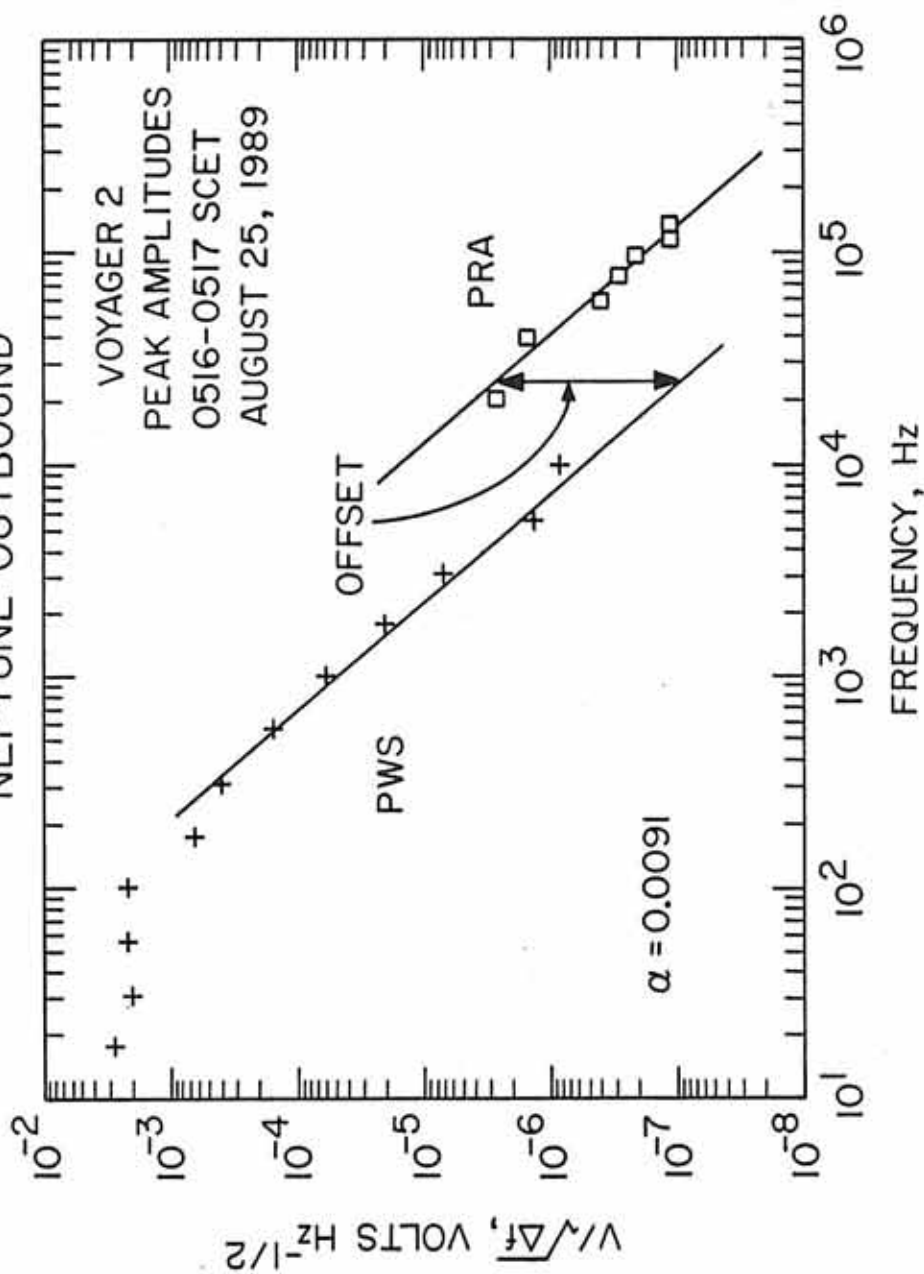
Figure 11.　The impact rate, R, from the wideband receiver and the best fit Gaussian profile (solid line). Note that R achieves its maximum value almost exactly at the equator crossing ($z = 0$). The error bars are 1 σ. The particle number density is shown in the right.

A-692-171-1

n, NUMBER DENSITY (m⁻³)
(A_S = 1.66 m²)

Z (km)
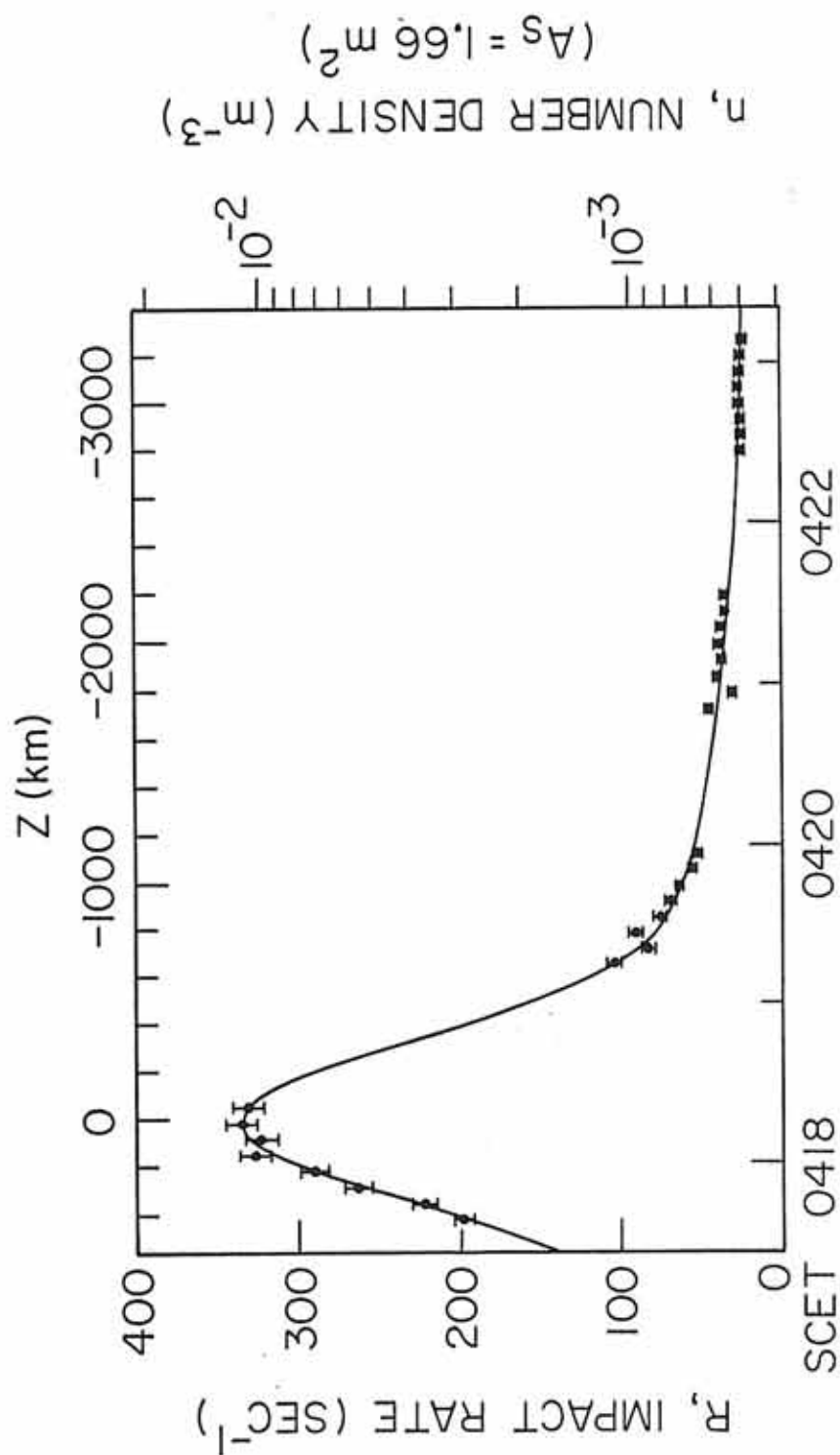
VOYAGER 2, AUGUST 26, 1981

R, IMPACT RATE (SEC⁻¹)

Figure 12.   The V_{rms} antenna voltage profile. Note that it becomes maximum at the equator crossing $(z = 0)$. The mass threshold scale is shown in the right.

A-G93-188-1
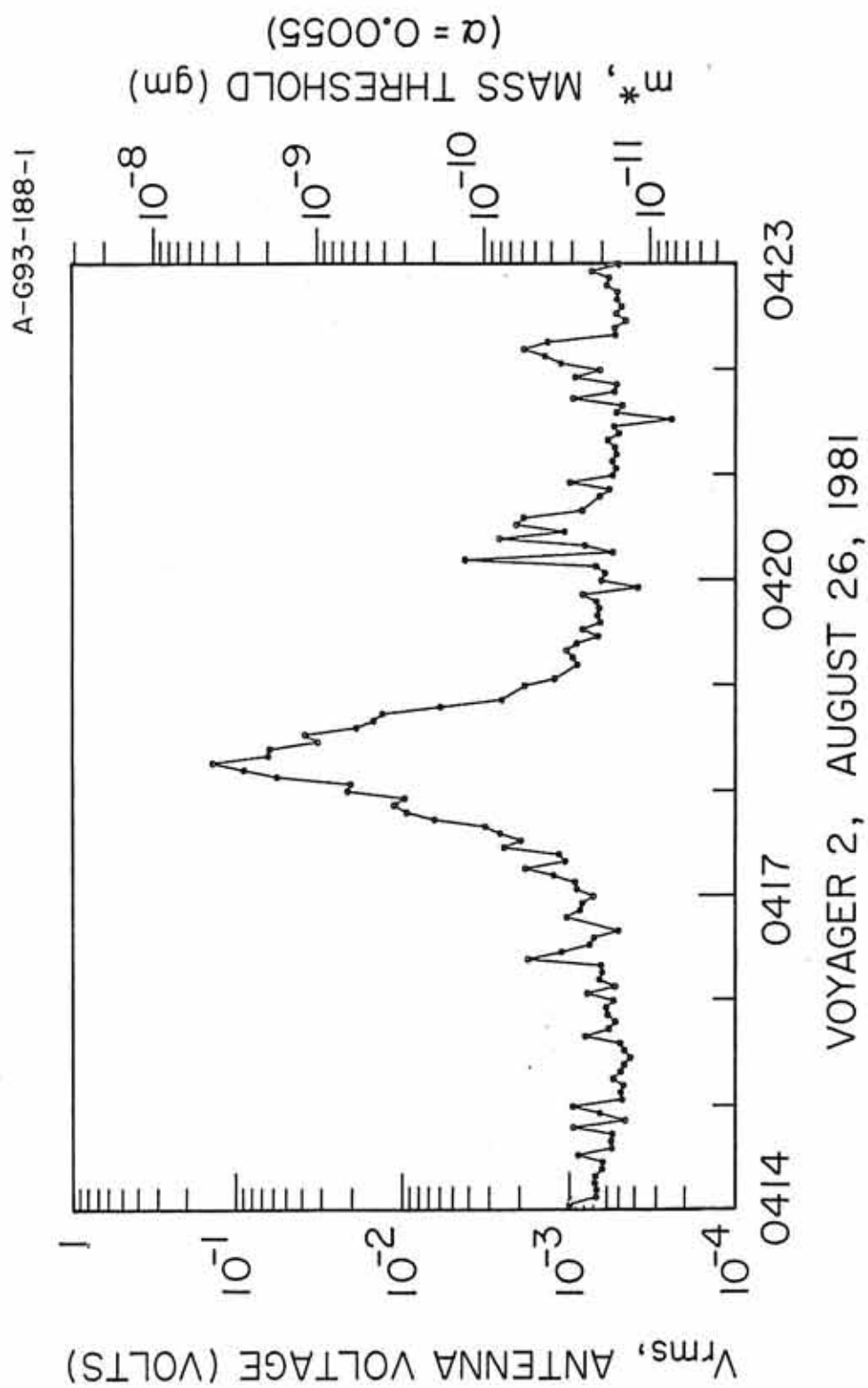
Figure 13. Comparison of the impact rate, R, and the rms antenna voltage, V_{rms}. R and V_{rms} can be analyzed to give the number density, n, and the mass threshold, m^*, respectively. The latter quantities can be seen on the right.

VOYAGER 2, AUGUST 26, 1981
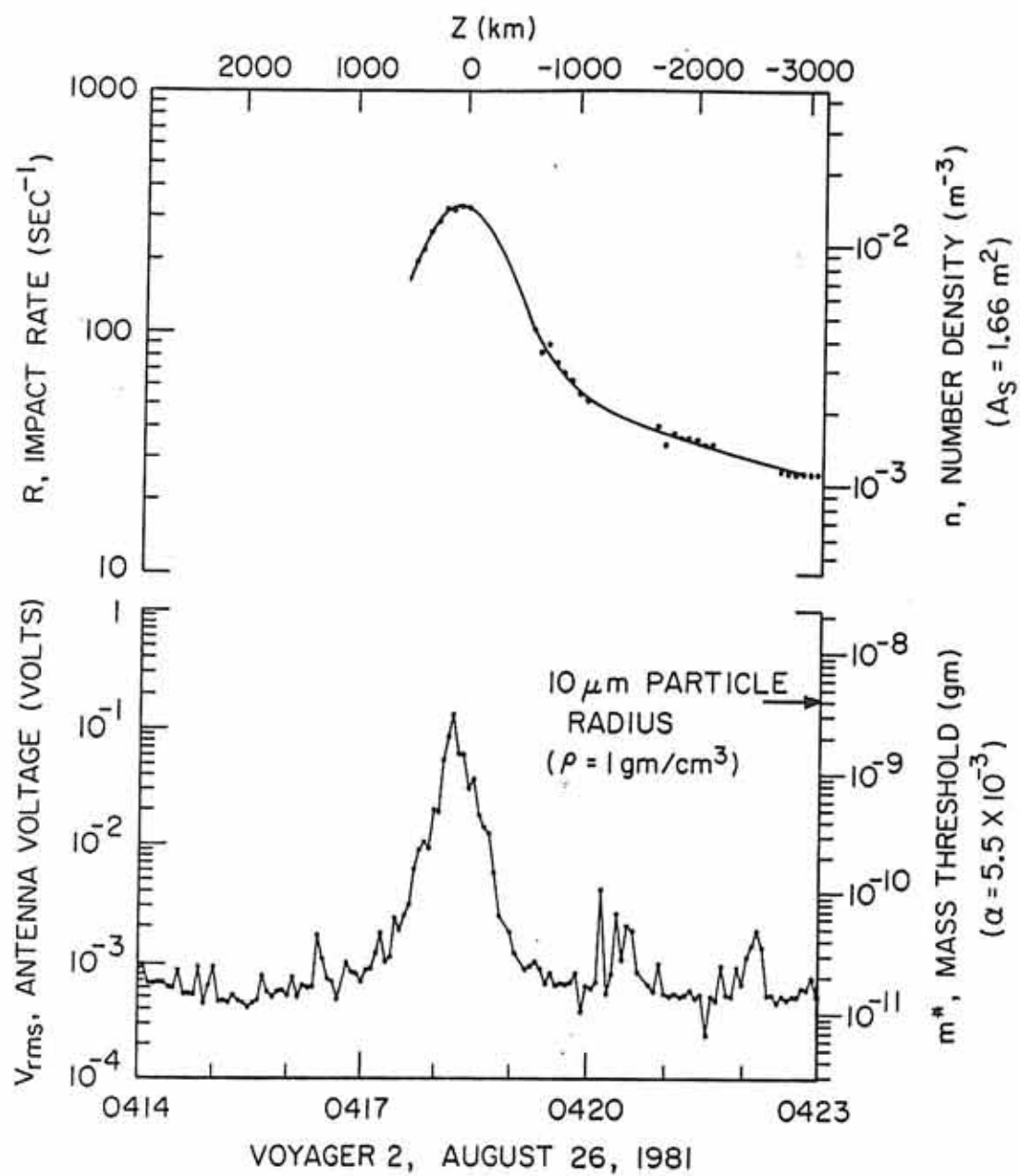
Figure 14. A summary of the observations of Voyager 1 at Saturn. The figure is adopted from Kurth and Gurnett [1991]. Among other features there is one labeled DUST? implying that dust impacts on the spacecraft may be at least partially responsible for the observed moise spectrum (see also Barbosa and Kurth [1993]).
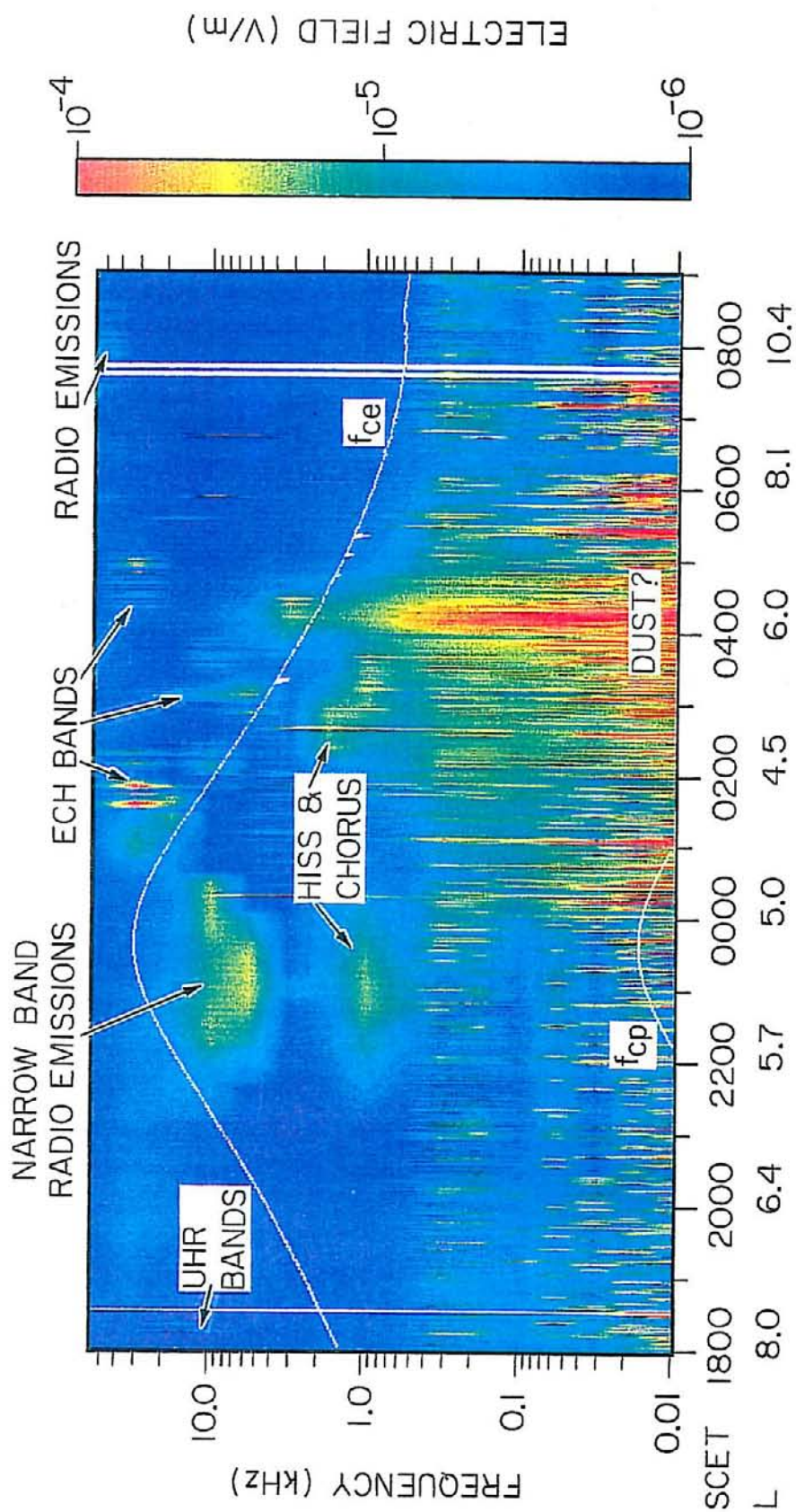
C-G9I-129-2

Figure 15.   The trajectory of Voyager 1 plotted in a meridional plane passing

through the spacecraft. The spacecraft crossed the equatorial plane at

6.24 R_S. The radial extent of some of the rings is also shown. The

circled A shows the position of the spacecraft when the last wideband

frame was taken before the equatorial plane crossing. The circled C.A.

shows the position of the spacecraft at closest approach: 3.05 R_S radial

distance and −39.51 degrees of latitude.

A-G92-230-1

VOYAGER I
E-RING
A-RING
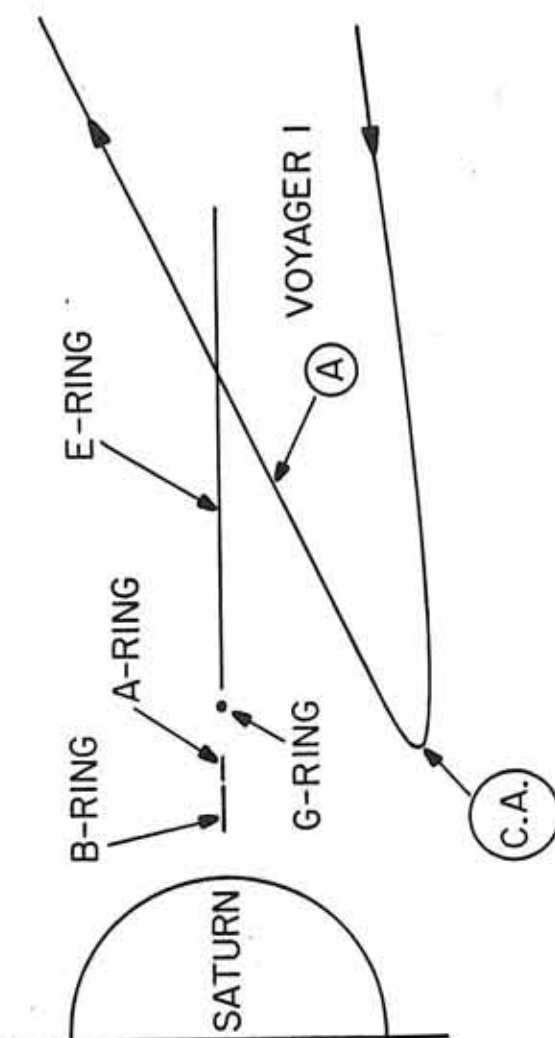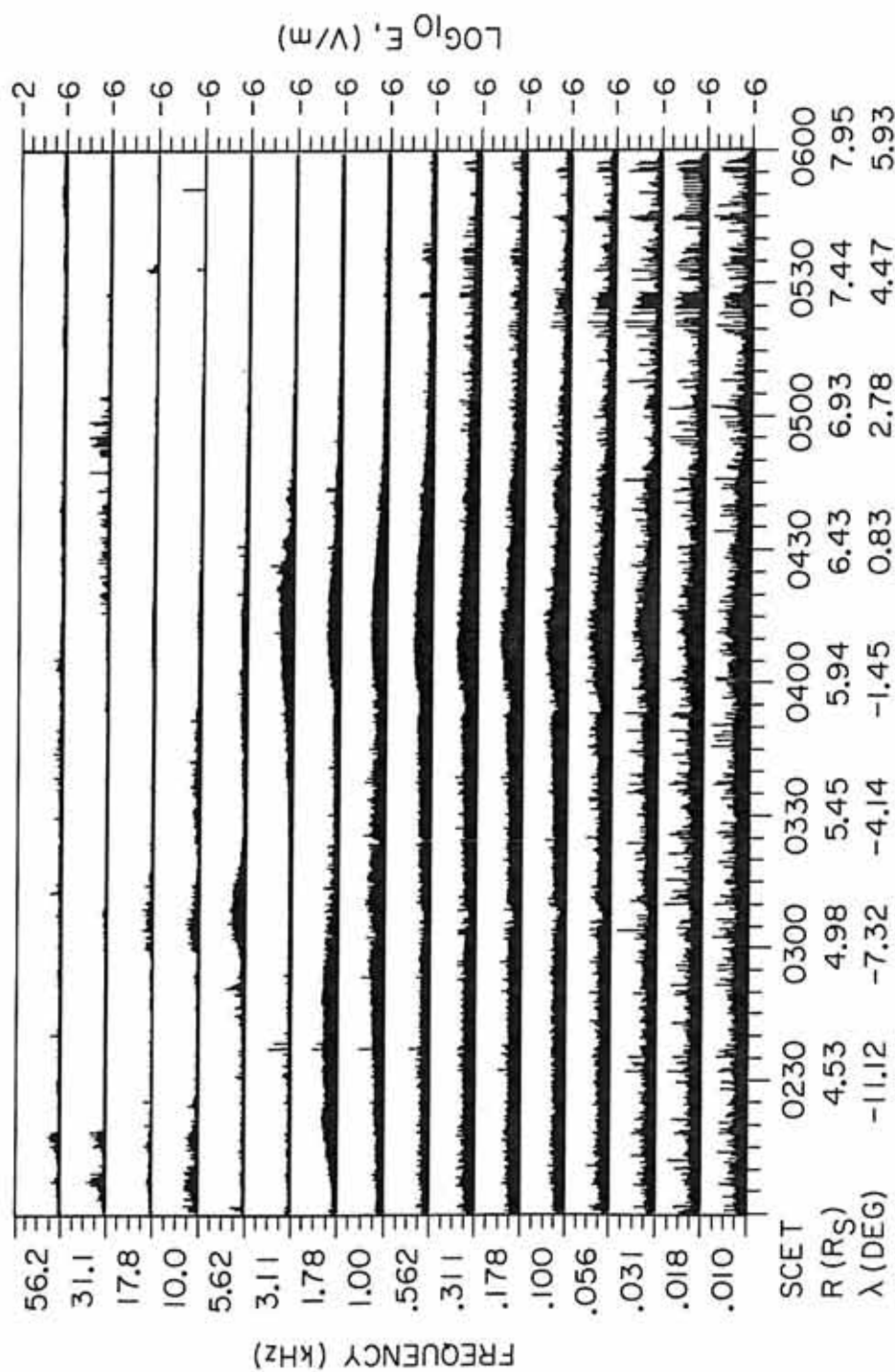B-RING
G-RING
SATURN
(A)
C.A.

Figure 16.   The Voyager 1 plasma wave observations 4 hours around the equatorial

plane crossing. Note the low-frequency enhancement from about 0400

to 0430 SCET.

VOYAGER I, NOVEMBER 13, DAY 318, 1980

Figure 17.   Frequency-time spectrogram for the Voyager 1 encounter with Saturn.

It is similar to Figure 2. Superimposed on the spectrogram is the profile

of the electron cyclotron frequency $f_{ce} = 28 \, |B|$. The frequency is in

Hz and the magnetic field is in nanoteslas. The most intense feature is

essentially a magnification (in time) of the feature tentatively labeled as

dust in Plate 3 of Kurth and Gurnett [1991].

C-G92-218-2

ELECTRIC FIELD (V/m)

10^{-4}

10^{-5}

10^{-6}

VOYAGER I   SATURN

NOVEMBER 13, DAY 318, 1980

f_{ce}

FREQUENCY (kHz)

10.0

1.0

0.1

0.01

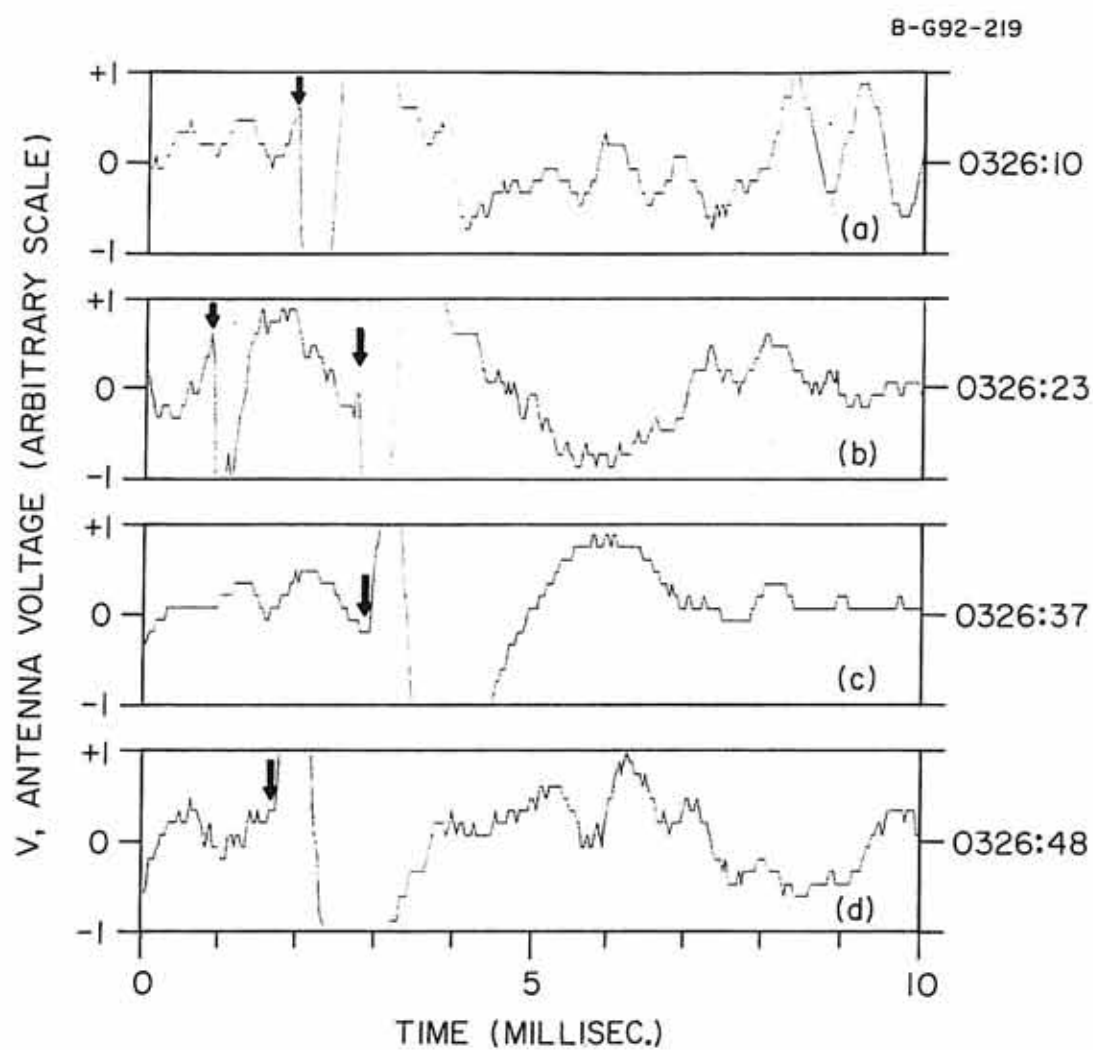| SCET	0330	0345	0400	0415	0430	0445
R(R_S)	5.45	5.69	5.94	6.18	6.43	6.68
λ(DEG)	-4.14	-2.74	-1.45	-0.26	0.83	1.84
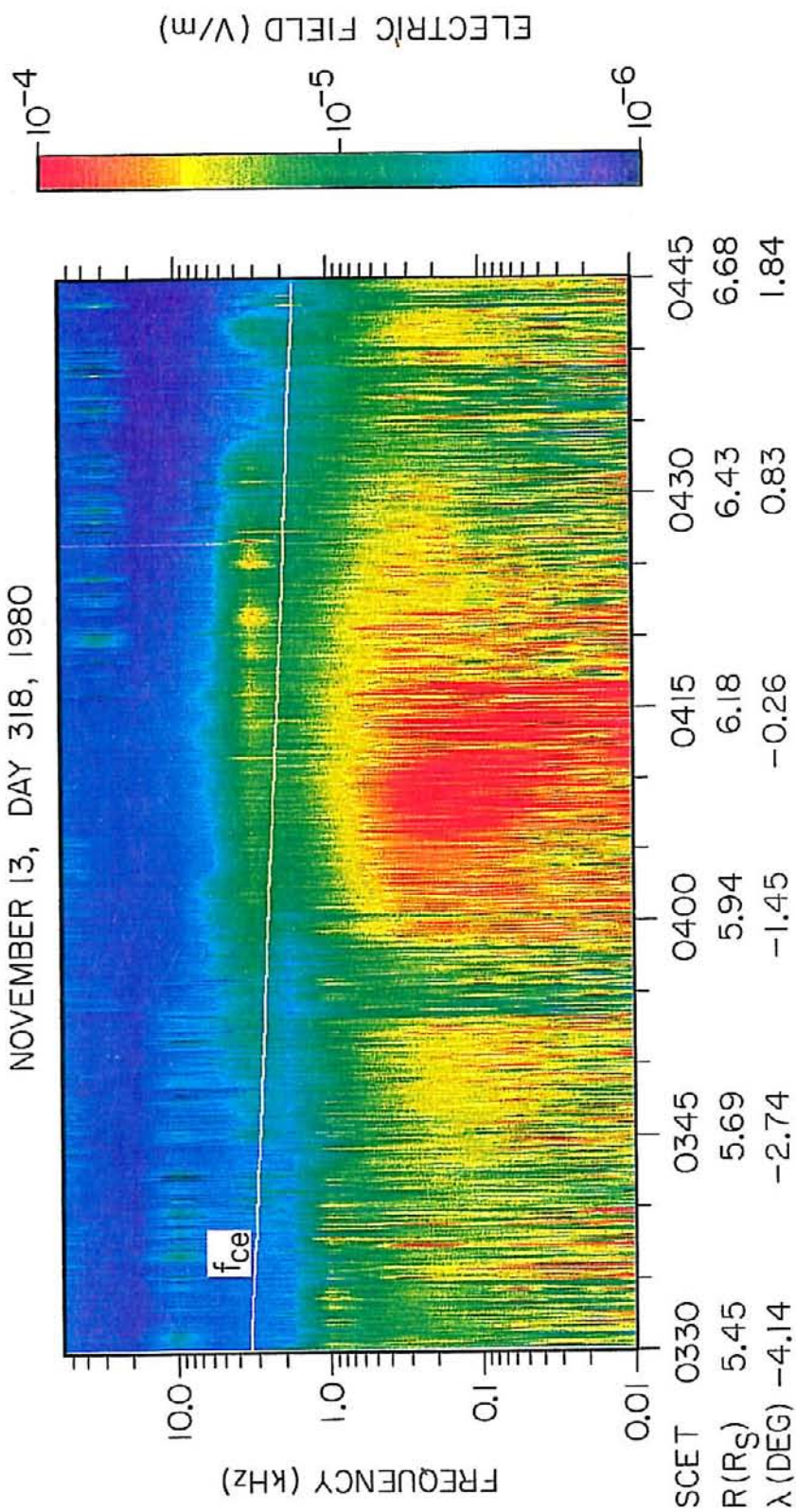
Figure 18.   A series of broadband waveforms of the particle impact noise taken at

0326 SCET when the spacecraft was at radial distance of 5.38 R_s and

latitude -4.53 degrees. The beginning of each impact is shown with an

arrow.

8-G92-219

VOYAGER 1, NOVEMBER 13, DAY 318, 1980

Figure 19.   The voltage spectrum during 0413 to 0414 SCET. This spectrum is for
the low-frequency equatorial enhancement shown in Figure 13. The
bump at higher frequencies corresponds to the relatively narrowband
feature above the electron cyclotron frequency (electron cyclotron
harmonic emission). It can easily be seen that at frequencies above a
few hundred Hertz the spectrum varies approximately as f^{-4}.

PEAK SPECTRUM

A-692-213

$$\frac{V^2}{\Delta f} \sim f^{-4}$$

SATURN
DUST IMPACTS
VOYAGER I
NOV. 13, DAY 318, 1980
SCET 0413-0414

FREQUENCY (Hz)

$\frac{V^2}{\Delta f}$, VOLTAGE SPECTRAL DENSITY
(VOLTS^2 Hz^{-1})

10^{-6} 10^{-8} 10^{-10} 10^{-12} 10^{-14}
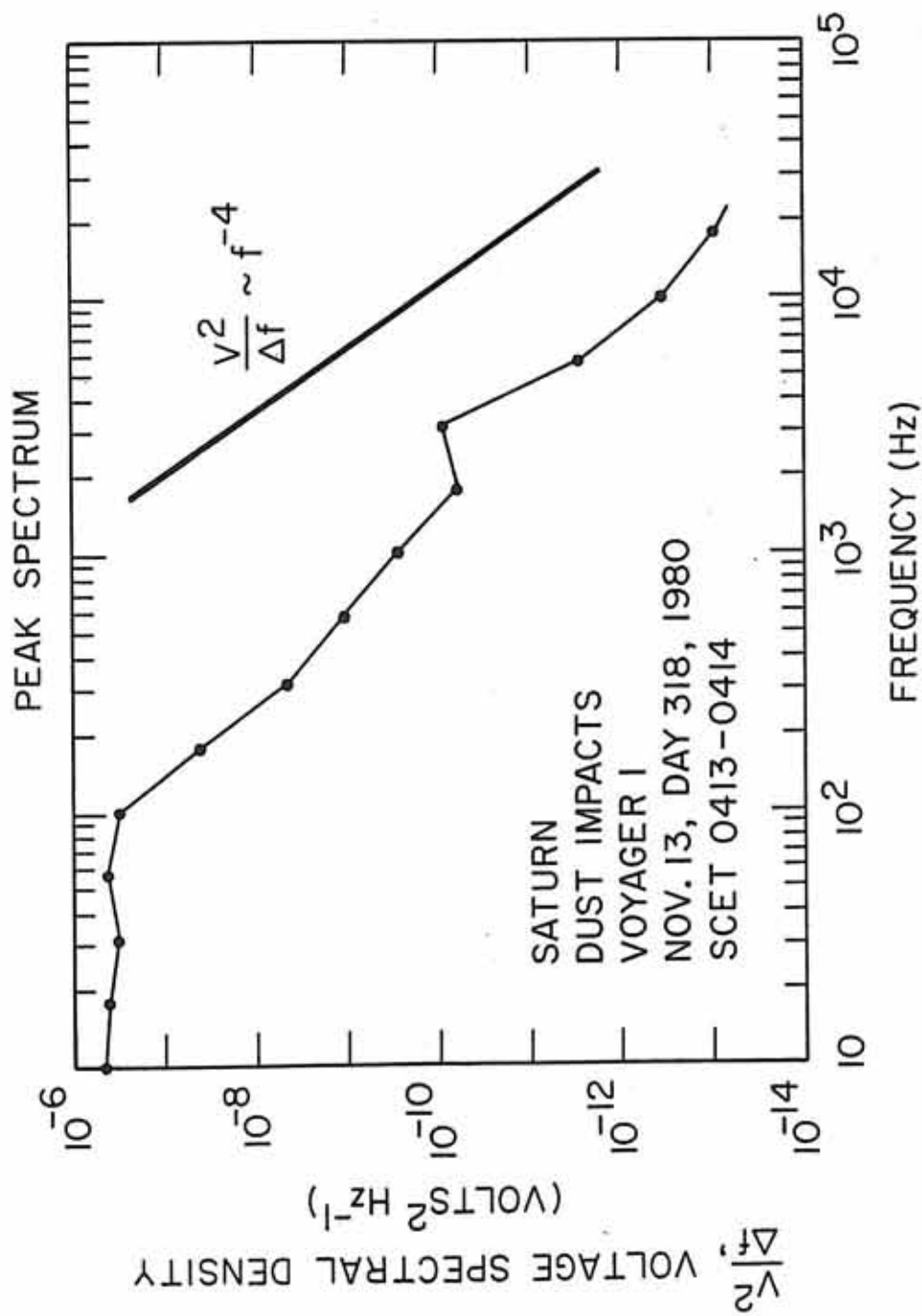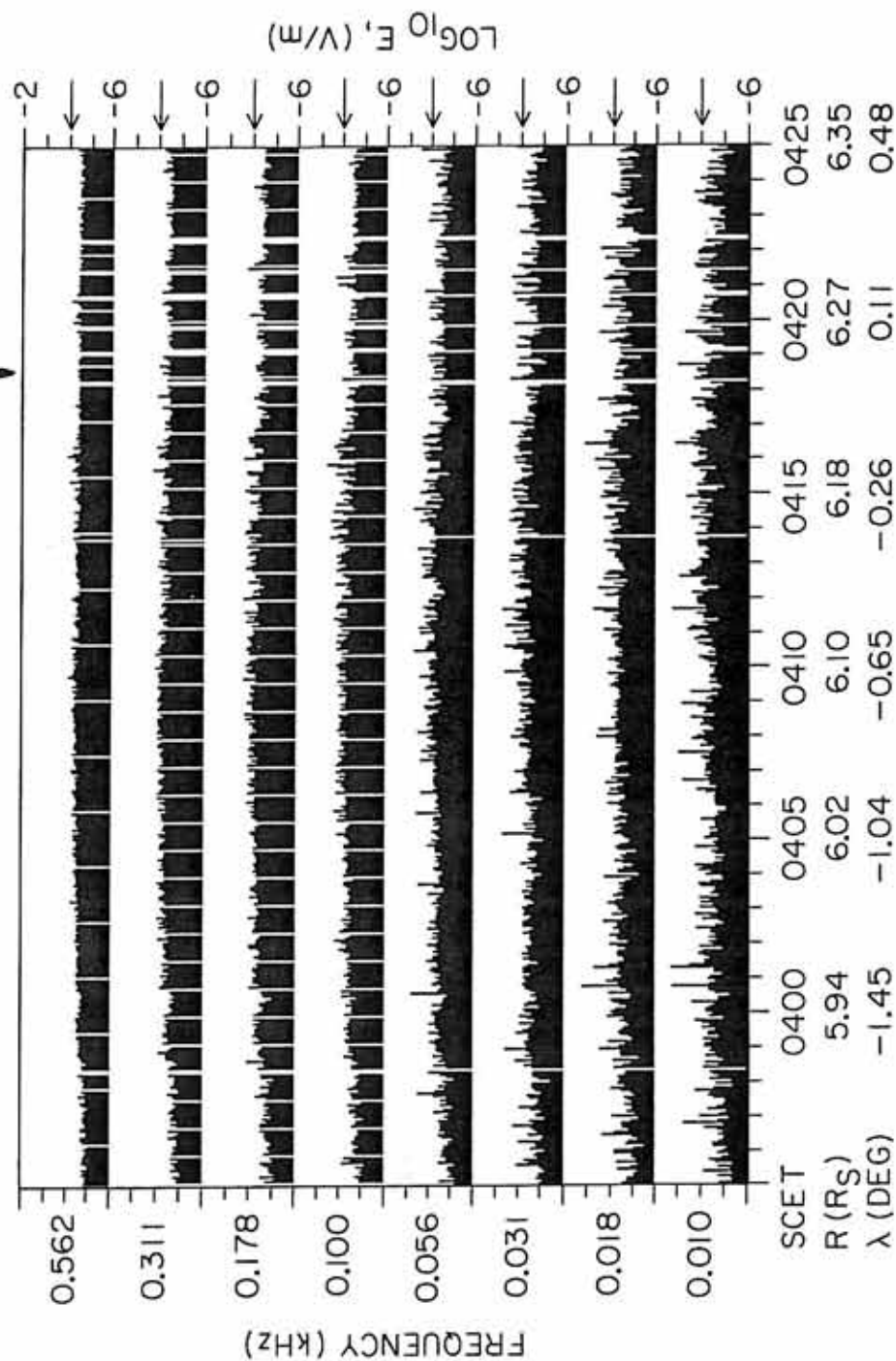
10 10^2 10^3 10^4 10^5

Figure 20. Voltages of the lowest 8 channels of the 16-channel spectrum analyzer as recorded near the equatorial plane. The position of the spacecraft is also shown at various times. Note that the intensity decreases as the frequency increases. Also note the bursty signals superimposed on the relatively smooth background.
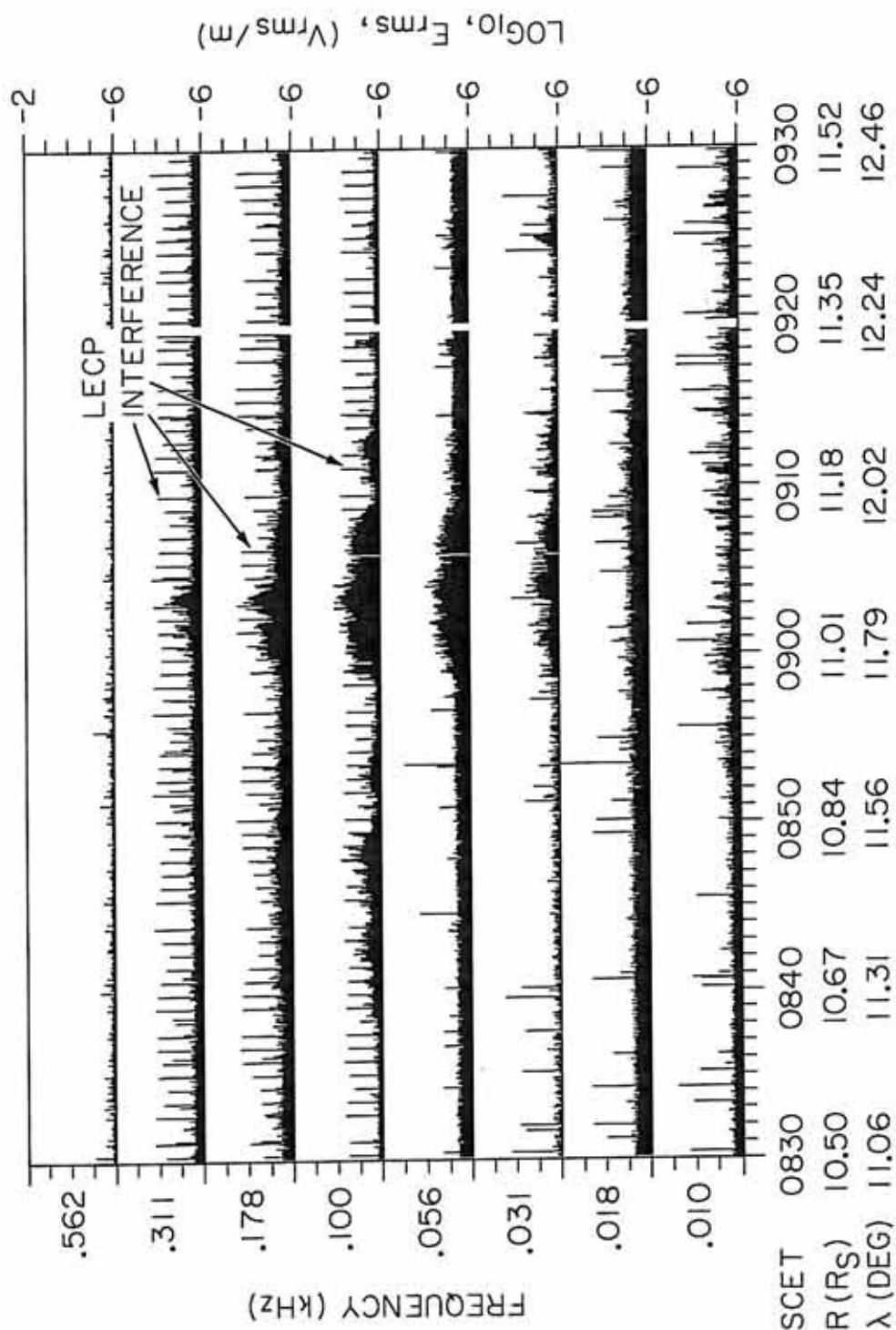
VOYAGER I, NOVEMBER 13, DAY 318, 1980

Figure 21.   LECP interference. The periodic spikes are attributed to the interference

caused by the Low Energy Charged Particles instrument.

VOYAGER 1, NOVEMBER 13, DAY 318, 1980

Figure 22.   A hypothetical distribution of the number of impacts with impact amplitude. Impact amplitude denotes the intensity of the signal and it depends on the particle mass, composition, speed, and impact geometry.
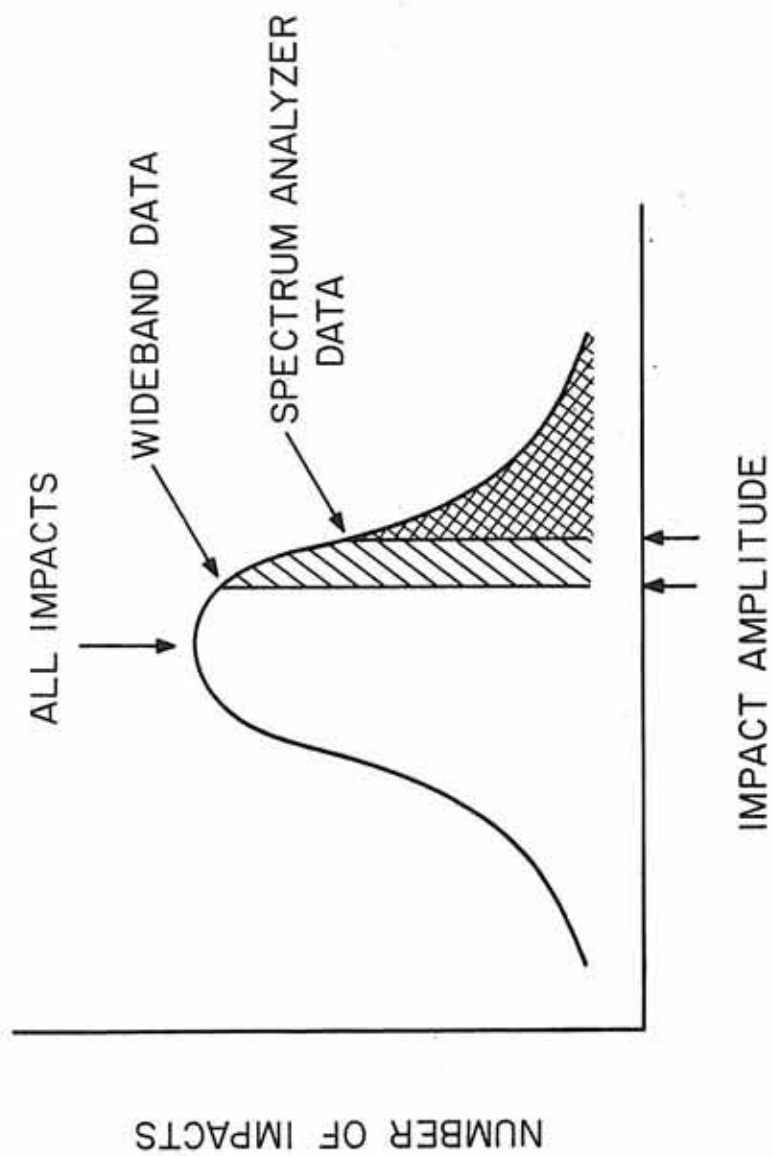
A-G93-280

Figure 23.   A comparison of the impact rates as deduced from the wideband data

and the 16-channel spectrum analyzer data. The later has already been

multiplied by the discrepancy factor of 28.3. The error bars are 1 σ.

A-G92-214-1

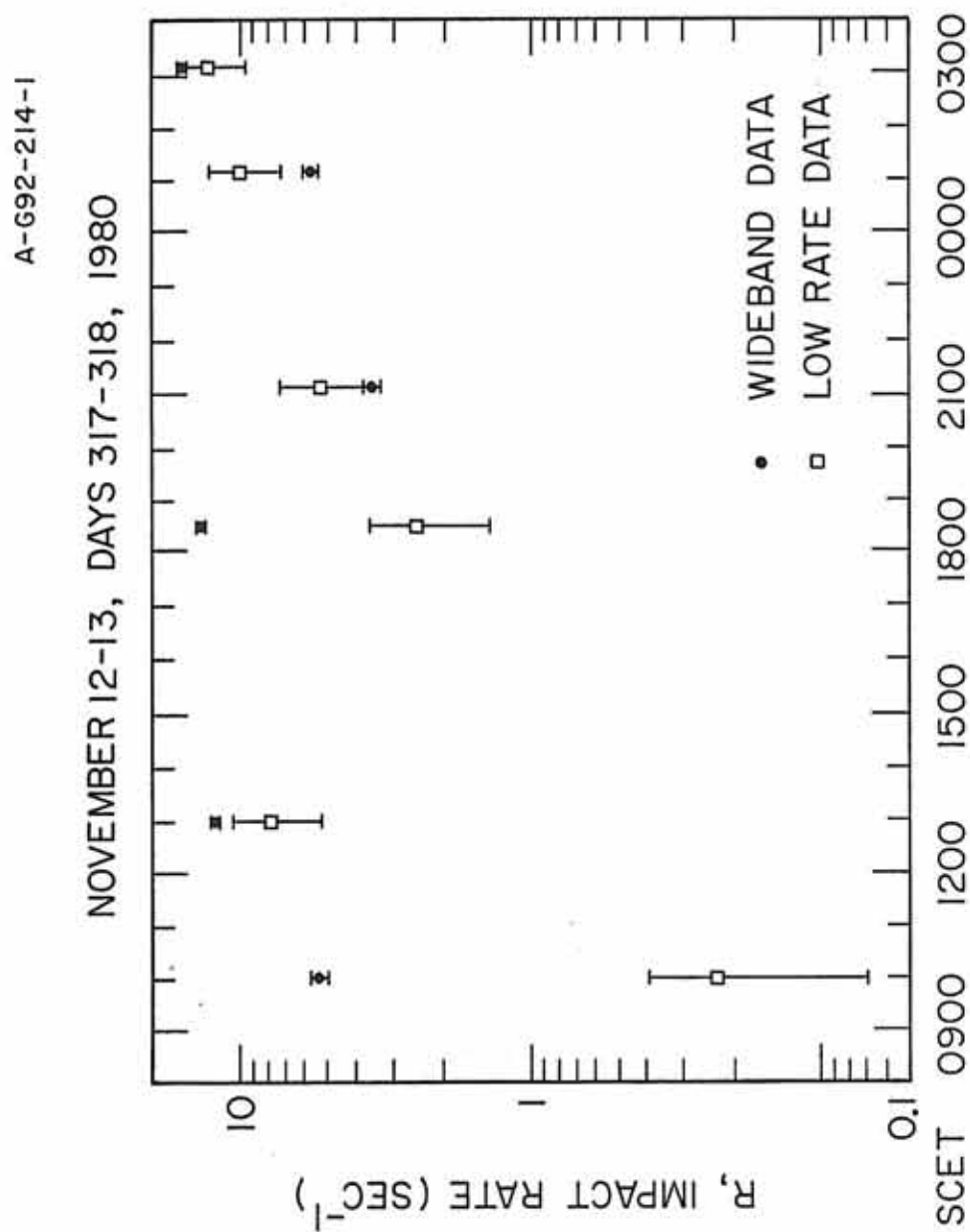NOVEMBER 12-13, DAYS 317-318, 1980

Figure 24.   The impact rate profile obtained from the 16-channel spectrum analyzer

data.   Note the clear peak centered at about 2500 km below the

equatorial plane crossing by the spacecraft.   The error bars are 1 σ.
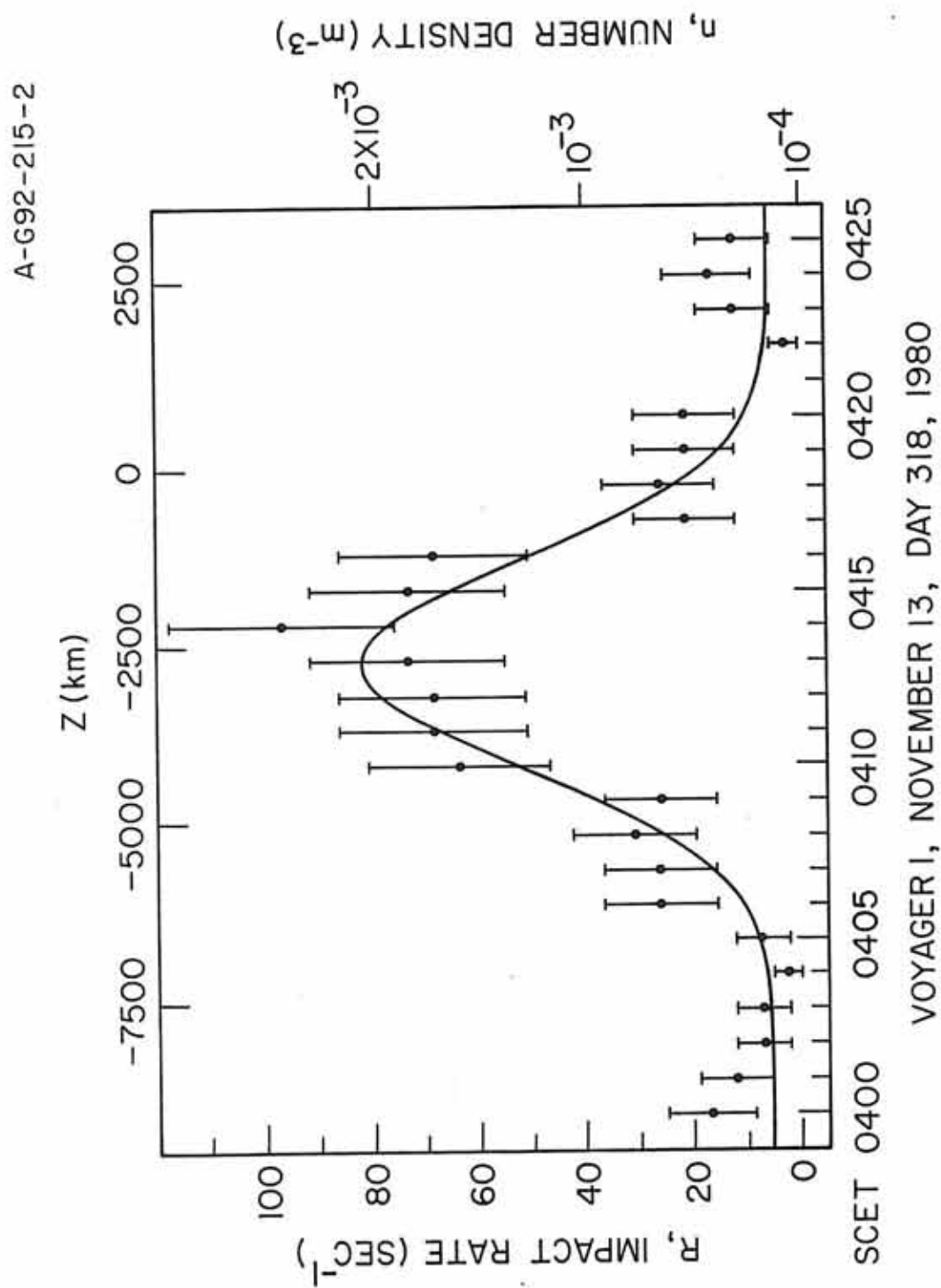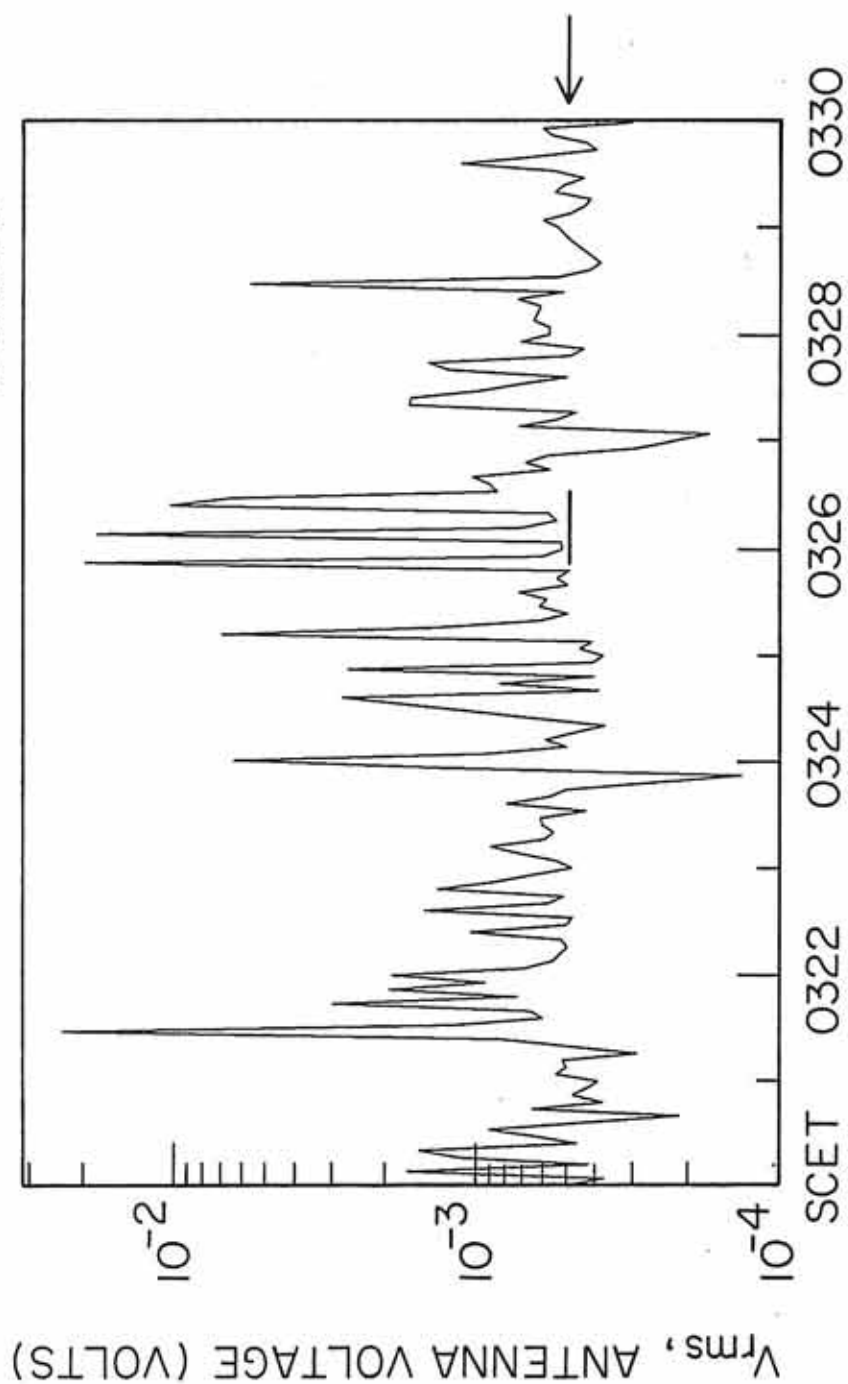
115

A-G92-215-2

Figure 25. The rms voltage profile a few minutes around 0326 SCET. The arrow indicates the voltage that corresponds to the wideband waveform receiver mass detection threshold. Basically the waveform receiver detects particles that are half a micron in size or more.

A-G93-346

Vrms, ANTENNA VOLTAGE (VOLTS)

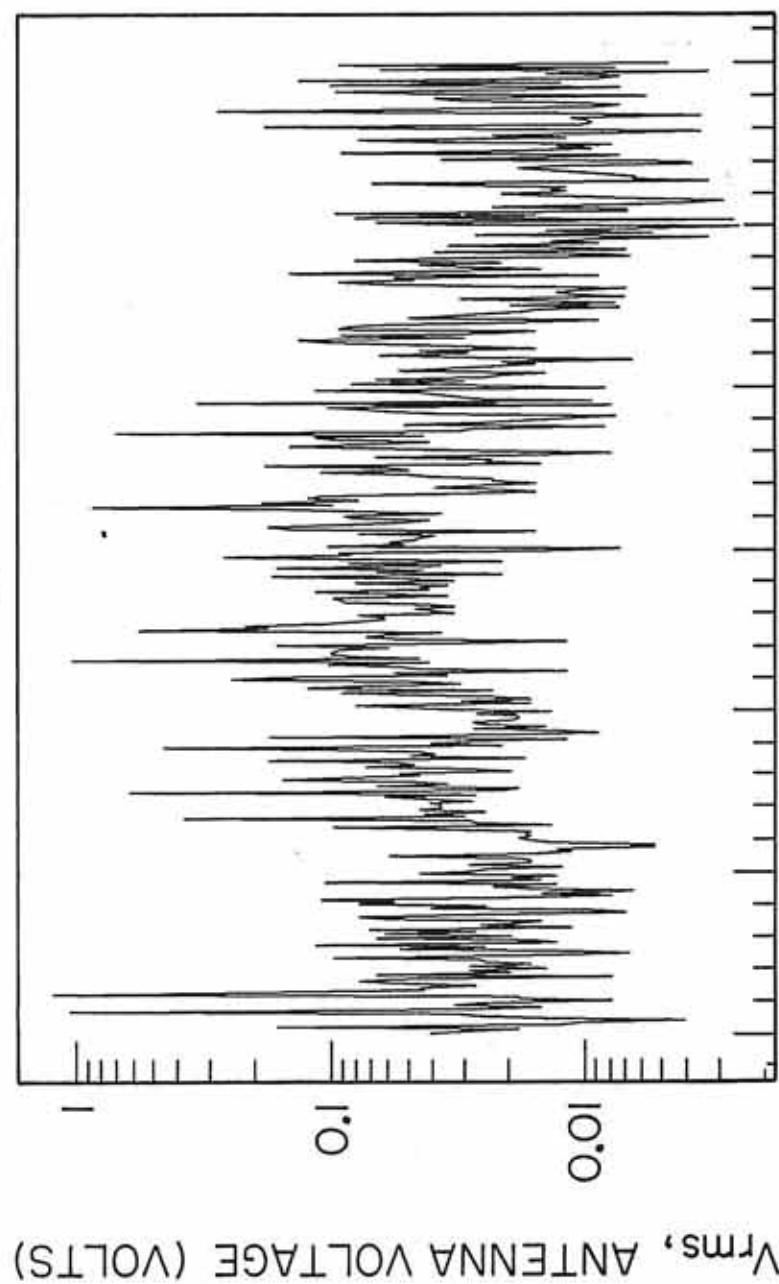SCET 0322 0324 0326 0328 0330

VOYAGER I, NOVEMBER 13, DOY 318, 1980

Figure 26.   The rms voltage profile for the first channel of Figure 20. If a typical

V_{rms} of 0.03 V is used in Equation (20) a particle radius of about 5

microns is obtained (dielectric particle).

A-693-347

10 Hz

SCET   0405   0415   0425

VOYAGER 1, NOVEMBER 13, DOY 318, 1981

Vrms, ANTENNA VOLTAGE (VOLTS)

Figure 27.   A summary of the results of the Voyager 1 and 2 encounters with the

Saturnian system. The regions where dust has been detected have been

exaggerated for purposes of clarity.

C-G93-189

A-RING   G-RING

B-RING

SATURN

VOYAGER 2

DIONE   TETHYS   ENCELADUS

VOYAGER I
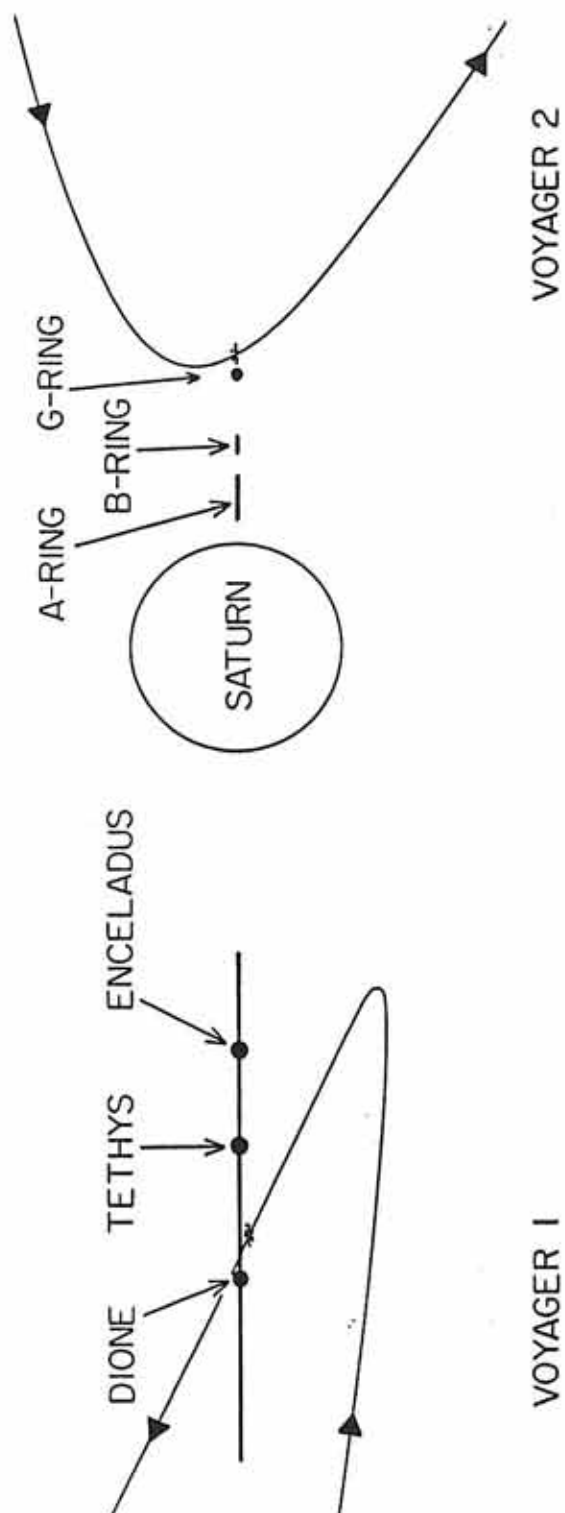
REFERENCES

Aubier, M. G., N. Meyer-Vernet, and B. M. Pedersen, Shot Noise from grain and particle impacts in Saturn's ring plane, Geophys. Res. Lett., 10, 5, 1983.

Barbosa, D. D., and W. S. Kurth, On the generation of plasma waves in Saturn's magnetosphere, J. Geophys. Res., 98, 9351, 1993.

Bridge, H. S., J. W. Belcher, A. J. Lazarus, S. Olbert, J. D. Sullivan, F. Bagenal, P. R. Gazis, R. E. Hartle, K. W. Ogilvie, J. D. Scudder, E. C. Sittler, A. Eviatar, G. L. Siscoe, C. K. Goertz, and V. M. Vasyliunas, Plasma Observations Near Saturn: Initial Results from Voyager 1, Science, 212, 217, 1981.

Bridge, H. S., F. Bagenal, J. W. Belcher, A. J. Lazarus, R. L. McNutt, J. D. Sullivan, P. R. Gazis, R. E. Hartle, K. W. Ogilvie, J. D. Scudder, E. C. Sittler, A. Eviatar, G. L. Siscoe, C. K. Goertz, and V. M. Vasyliunas, Plasma observations Near Saturn: Initial Results from Voyager 2, Science, 215, 563, 1982.

Burns, J. A., M. R. Showalter, and G. E. Morfill, The ethereal rings of Jupiter and Saturn, in Planetary Rings, edited by R. Greenbery and A. Brahic, pp. 200-272, University of Arizona Press, Tucson, 1984.

Connerney, J. E. P., N. F. Ness, and M. H. Acuña, Zonal harmonic model of Saturn's magnetic field from Voyager 1 and 2 observations, Nature, 298, 44-46, 1982.

Esposito, L. W., J. N. Cuzzi, J. B. Holberg, E. A. Marouf, G. L. Tyler, and C. C. Porco, Saturn's rings: Structure, dynamics, and particle properties, in Planetary Rings, edited by T. Gehrels and M. S. Matthews, pp. 463-545, University of Arizona Press, Tucson, 1984.

Fechtig, H., E. Grün, and J. Kissel, Laboratory simulations. In Cosmic Dust, edited by J. A. M. McDonnell, John Wiley, New York, 1978.

Goertz, C. K., G. E. Morfill, W. Ip, E. Grün, and O. Havnes, Electromagnetic angular momentum transport in Saturn's rings, Nature, 320, 141, 1986.

Grün, E., Experimental studies of impact ionization, Eur. Space Agency Spec. Publ., SP-155, 81, 1984.

Grün, E., G. E. Morfill, and D. A. Mendis, Dust-magnetosphere interactions, in Planetary Rings, edited by R. Greenbery and A. Brahic, pp. 275-332, University of Arizona Press, Tucson, 1984.

Gurnett, D. A., W. S. Kurth, and F. L. Scarf, Plasma waves near Saturn: Initial results from Voyager 1, Science, 212, 235, 1981.

Gurnett, D. A., E. Grün, D. Gallagher, W. S. Kurth, and F. L. Scarf, Micron sized particles detected near Saturn by the Voyager plasma wave instrument, Icarus, 53, 236, 1983.

Gurnett, D. A., W. S. Kurth, F. L. Scarf, J. A. Burns, J. N. Cuzzi, and E. Grün, Micron-sized particles detected near Uranus by the Voyager plasma wave instrument, J. Geophys. Res., 92, 14,959, 1987.

Gurnett, D. A., W. S. Kurth, L. J. Granroth, S. C. Allendorf, and R. L. Poynter, Micron-sized particles detected near Neptune by the Voyager plasma wave instrument, J. Geophys. Res., 96, 19,177, 1991.

Hamilton, D. P., Motion of Dust in a Planetary Magnetosphere: Orbit-Averaged Equations for oblateness, electromagnetic, and radiation forces with application to Saturn's E ring, Icarus, 101, 244, 1993.

Horanyi, M., J. A. Burns, and D. P. Hamilton, The dynamics of the Saturn E ring particles, Icarus, 97, 248, 1992.

Hornung, K., and S. Drapatz, Residual ionization after impact of large dust particles, The comet Halley probe environment, Eur. Space Agency Spec. Publ., SP-155, 23, 1981.

Humes, D. H., Results of Pioneer 10 and 11 meteoroid experiments: Interplanetary and near Saturn, J. Geophys. Res., 85, 5841, 1980.

Kurth, W. S., D. A. Gurnett, and F. L. Scarf, A search for Saturn electrostatic discharges in the Voyager plasma wave data, Icarus, 53, 255, 1983.

Kurth, W. S., and D. A. Gurnett, Plasma waves in planetary magnetospheres, J. Geophys. Res., 96, 18977, 1991.

McDonnell, J. A. M., Microparticle studies by space instrumentation. In Cosmic Dust, edited by J. A. M. McDonnell, John Wiley, New York, 1978.

Meyer-Vernet, N., and C. Perche, Tool kit for antennae and thermal noise near the plasma frequency, J. Geophys. Res., 94, 2405, 1989.

Ness, N. F., M. H. Acuña, R. P. Lepping, J. E. P. Connerney, K. W. Behannon, L. F. Burlaga, and F. M. Neubauer, Magnetic field studies by Voyager 1: Preliminary results at Saturn, Science, 212, 211, 1981.

Ness, N. F., M. H. Acuña, K. W. Behannon, L. F. Burlaga, J. E. P. Connerney, R. P. Lepping, and F. M. Neubauer, Magnetic field Studies by Voyager 2: Preliminary results at Saturn, Science, 215, 558, 1982.

Northrop, T.G., and J. R. Hill, The adiabatic motion of charged dust grains in rotating magnetospheres, J. Geophys. Res., 88, 1, 1983.

Press, W. H., B. P. Flannery, S. A. Teukolsky, and W. T. Vetterling, Numerical Recipes (Fortran), Chapter 14, published by Cambridge University Press, New York, 1989.

Randall, B. A., Energetic electrons in the magnetosphere of Saturn, to be submitted to J. Geophys. Res., 1993.

Scarf, F. L, and D. A. Gurnett, A plasma wave investigation for the Voyager mission, Space Sci. Rev., 21, 289, 1977.

Scarf, F. L., D. A. Gurnett, W. S. Kurth, and R. L. Poynter, Voyager 2 plasma wave observations at Saturn, Science, 215, 287, 1982.

Scarf, F. L, D. A. Gurnett, W. S. Kurth, and R. L. Poynter, Voyager plasma wave measurements at Saturn, J. Geophys. Res., 88, 8971, 1983.

Schaffer, L., and J. A. Burns, The dynamics of weakly charged dust: Motion through Jupiter's gravitational and magnetic fields, J. Geophys. Res., 92, 2264, 1987.

Sheehan, D. P., C. A. Casey, and L. T. Volz, Interaction of an expanding plasma cloud with a simple antenna-application to anomalous voltage signals observed by Voyager 1, Voyager 2, and ICE spacecraft, submitted to J. Geophys. Res., 1992.

Showalter, M. R., J. N. Cuzzi, and S. M. Larson, Structure and particle properties of Saturn's E ring, Icarus, 94, 451, 1991.

Showalter, M. R., and J. N. Cuzzi, Seeing ghosts: Photometry of Saturn's G ring, Icarus, 103, 124, 1993.

Smith, B. A., L. Soderblom, R. Beebe, J. Boyce, G. Briggs, A. Bunker, S. A. Collins, C. J. Hansen, T. V. Johnson, J. L. Mitchell, R. J. Terrile, M. Carr, A. F. Cook II, J. N. Cuzzi, J. B. Pollack, G. E. Danielson, A. Ingersoll, M. E. Davies, G. E. Hunt, H. Masursky, E. Shoemaker, D. Morrison, T. Owen, C. Sagan, J. Veverka, R. Strom, and V. E. Suomi, Encounter with Saturn: Voyager 1 imaging science results, Science, 212, 163, 1981.

Smith, B. A., L. Soderblom, R. Batson, P. Bridges, J. Inge, H. Masursky, E. Shoemaker, R. Beebe, J. Boyce, G. Briggs, A. Bunker, S. A. Collins, C. J. Hansen, T. V. Johnson, J. L. Mitchell , R. J. Terrile, A. F. Cook II, J. N. Cuzzi, J. B. Pollack, G. E. Danielson, A. P. Ingersoll, M. E. Davies, G. E. Hunt, D. Morrison, T. Owens, C. Sagan, J. Veverka, R. Strom, and V. E. Suomi, A new look at the Saturn system: The Voyager 2 images, Science, 215, 504, 1982.

Stone, E. C., and E. D. Miner, Voyager 1 Encounter with the Saturnian System, Science, 212, 159, 1981.

Stone, E. C., and E. D. Miner, Voyager 2 Encounter with the Saturnian System, Science, 215, 499, 1982.

Tsintikidis, D., D. A. Gurnett, L. J. Granroth, S. C. Allendorf, and W. S. Kurth, A revised analysis of micron-sized particles near Saturn by the Voyager 2 plasma wave instrument, submitted to J. Geophys. Res., 1993.

Warwick, J. W., J. B. Pearce, D. R. Evans, T. D. Carr, J. J. Schauble, J. K. Alexander, M. L. Kaiser, M. D. Desch, M. Pedersen, A. Lecacheux, G. Daigne, A. Boischot, and C. H. Barrow, Planetary radio astronomy observations from Voyager 1 near Saturn, Science, 212, 239, 1981.

Warwick, J. W., D. R. Evans, J. H. Romig, J. K. Alexander, M. D. Desch, M. L. Kaiser, M. Aubier, Y. Leblanc, A. Lecacheux, and B. M. Pedersen, Planetary radio astronomy observations from Voyager 2 near Saturn, Science, 215, 582, 1982.